We turn anomaly hunting among 373,646 variable stars from manual triage into a fast, affordable active-learning search.

Draft version August 26, 2026
Typeset using LaTeX **twocolumn** style in AASTeX7.0.1

arXiv:2608.23688v1 [astro-ph.SR] 24 Aug 2026

Agentic Active Learning Meets Visual Embeddings: Finding Anomalies among 370 000 Variable Stars from ASAS-SN

Milan Pešta[1,2,3] and Yuan-Sen Ting[2,3,4]

[1] *Institute of Theoretical Physics, Faculty of Mathematics and Physics, Charles University, V Holešovičkách 2, 180 00 Prague, Czech Republic*
[2] *Department of Astronomy, The Ohio State University, 140 West 18th Avenue, Columbus, OH, 43210, USA*
[3] *Center for Cosmology and AstroParticle Physics, The Ohio State University, 191 West Woodruff Avenue, Columbus, OH 43210, USA*
[4] *Max-Planck-Institut für Astronomie, Königstuhl 17, D-69117 Heidelberg, Germany*

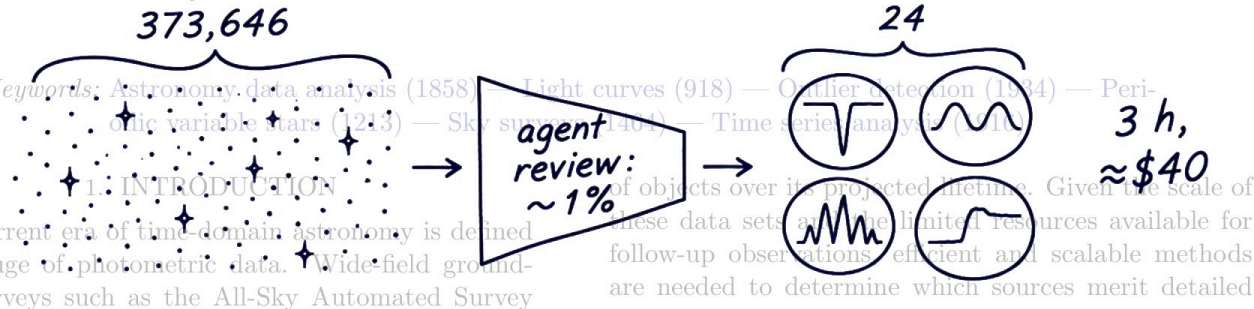
ABSTRACT

The key move is asking agents to inspect only candidates that the evolving search considers useful.

Unusual light-curve morphologies can point to rare physical configurations or new phenomena, but automatic searches for anomalies are often dominated by artifacts. Separating genuine anomalies from false positives has traditionally required manual vetting, which does not scale to modern surveys. We present an active learning framework for detecting anomalies in samples of periodic variable stars, with the vetting delegated to multimodal large language model agents. The initial ranking comes from isolation forests trained on DINOv2 ViT-g/14 embeddings of phase-folded light curves. The agents iteratively review the light-curve images of the top-ranked candidates and assign relevance scores, which are propagated through the embedding space to prioritize the next targets. A logistic regression step then extends the search beyond label propagation, and a multi-agent consensus review filters false positives. Using Gemini 3 Flash agents, we applied the pipeline to 373 646 periodic variables from ASAS-SN Sky Patrol V2.0. Across 51 iterations, the agents labeled ∼1% of the sample in roughly 3 hours at a cost of ≈$40, yielding our final catalog of 24 anomalies (18 newly reported) and 153 potentially interesting objects. The anomalies include eclipsing binaries with extremely deep primary eclipses, high-amplitude contact binaries and pulsators, and a symbiotic nova in outburst for over two decades. At the same labeling budget, the initial ranking would have recovered only 30% of our catalog, while reaching its lowest-ranked anomaly would have required ∼70 times the budget. These results demonstrate the feasibility of agentic active learning for anomaly hunting in large photometric surveys.

No astronomy-specific fine-tuning was needed; both the visual encoder and LLM were used off the shelf.

The practical result: roughly 1% reviewed, 24 anomalies retained, and 18 newly reported.



Keywords: Astronomy data analysis (1858) — Light curves (918) — Outlier detection (1934) — Periodic variable stars (1213) — Sky surveys (1464) — Time series analysis (1916)

1. INTRODUCTION

The current era of time-domain astronomy is defined by a deluge of photometric data. Wide-field ground-based surveys such as the All-Sky Automated Survey for SuperNovae (ASAS-SN; B. J. Shappee et al. 2014; C. S. Kochanek et al. 2017) and the Zwicky Transient Facility (ZTF; E. C. Bellm et al. 2019) provide multi-epoch observations for hundreds of millions of sources. The upcoming Vera C. Rubin Observatory Legacy Survey of Space and Time (LSST; Ž. Ivezić et al. 2019) will expand this further, delivering light curves for billions of objects over its projected lifetime. Given the scale of these data sets and the limited resources available for follow-up observations, efficient and scalable methods are needed to determine which sources merit detailed examination.

Anomalies are a natural target for such prioritization. These objects deviate from typical source types and behaviors, which can point to extreme physical conditions or new phenomena. Historically, many discoveries have emerged from examining sources that defied initial classification or showed unusual behavior (e.g., A. Hewish et al. 1968; M. Schmidt 1963; H. S. Leavitt & E. C. Pickering 1912). Identifying anomalies in large surveys is therefore essential for testing theoretical models and uncovering exotic objects.

Corresponding author: Milan Pešta
pesta.22@osu.edu

Unsupervised searches find instrumental oddities as readily as astrophysical ones, so judgment—not ranking—is the real bottleneck.

Several unsupervised methods for anomaly detection are commonly used in the literature. Techniques such as isolation forests (F. T. Liu et al. 2008; V. A. Villar et al. 2021), autoencoders (G. E. Hinton & R. R. Salakhutdinov 2006; C. Nicolaou et al. 2026), and normalizing flows (D. Jimenez Rezende & S. Mohamed 2015; Y. Liang et al. 2023) can identify outliers without requiring predefined labels. However, their effectiveness depends strongly on how the data is represented. In the case of light curves, manually curated features such as Fourier coefficients, color indices, and light-curve statistics are effective for population studies and classification (e.g., N. Christo[illegible] 1[illegible] Bloemen et al. 2011; Debosscher et al. 2007; D. W. Kim et al. 2014; C. A. L. Pastor-Marazuela et al. 2026), but they may not capture the subtle morphological nuances that distinguish unusual objects from standard sources. If the representation is not sensitive to the relevant form of anomalous behavior, such sources can remain hidden within the bulk distribution.

Visual embeddings preserve morphology that a short list of hand-crafted statistics can miss.

An alternative is to represent each light curve by its visual appearance rather than a fixed set of hand-crafted features. Vision foundation models trained on large collections of natural images, such as CLIP (A. Radford et al. 2021), MAE (K. He et al. 2021), and DINOv2 (M. Oquab et al. 2023), learn general-purpose representations that transfer to new domains with little or no fine-tuning. Applied to light-curve images, they capture both the global morphology and local irregularities, such as asymmetries, scatter, and phase-dependent features. Visual embeddings have proven effective for light-curve classification tasks (D. Moreno-Cartagena et al. 2025), but remain largely unexplored for anomaly detection.

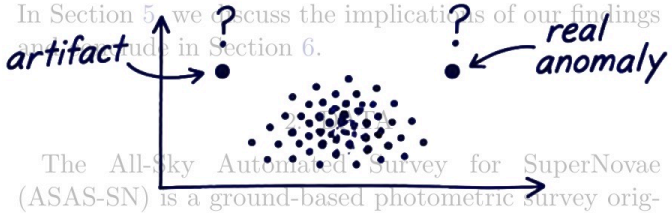
In practice, even a representation that preserves the anomalous structure of light curves can yield unsupervised models that favor instrumental artifacts over genuine astrophysical anomalies, since these contaminants also appear as outliers in the data. The scale of this contamination can be severe. For instance, V. Etsebeth et al. (2024) applied isolation forests to ∼4 million galaxy images from the Dark Energy Camera Legacy Survey (DECaLS) and found that 1 763 of the top 2 000 candidates were instrumental artifacts or masked sources, with only a single scientifically interesting anomaly present in the initial ranking.

A malformed light curve can be more isolated than a genuinely exotic star.

Removing such contaminants traditionally requires labor-intensive human vetting, which does not scale to modern survey sizes. Active learning mitigates this by directing expert review only to the most informative candidates (M. Lochner & B. A. Bassett 2021; M. Lochner & L. Rudnick 2025), sharply reducing the labeling effort needed to separate artifacts from genuine anomalies. However, when expert time is scarce or the labeling effort must be regularly repeated, even active learning becomes prohibitive. The labor bottleneck could be relieved by large language models (LLMs), which have been shown to perform well in a variety of contexts (e.g., F. Stoppa et al. 2025; M. Jia et al. 2026; D. Ferber et al. 2024; X. Xu et al. 2025), yet active learning applications in astronomy have so far relied on human experts (e.g., M. Leoni et al. 2022; E. E. O. Ishida et al. 2019; J. W. Richards et al. 2012; M. Lochner & B. A. Bassett 2021; E. E. O. Ishida et al. 2021; M. V. Pruzhinskaya et al. 2023).

In this work, we introduce an active learning framework for anomaly detection in which LLM agents[†] take over the expert role, and demonstrate its feasibility on a sample of over 370 000 periodic variable stars from the ASAS-SN survey. The active learning aspect is central to our approach, as evaluating every source with an LLM agent would be too costly at survey scale. Our pipeline derives an initial anomaly ranking from isolation forests trained on visual embeddings of the light curves, which we obtain using an off-the-shelf vision model without any fine-tuning or survey-specific adaptation. LLM agents then iteratively refine this ranking through active learning, and the resulting labels feed a classifier search and a final multi-agent consensus review of all candidates. Together, these steps form an automated workflow for systematic anomaly detection that is no longer limited by expert availability.

The paper is organized as follows. In Section 2, we describe the ASAS-SN data and our sample selection. We detail the pipeline in Section 3 and present the discovery statistics and the anomaly catalog in Section 4. In Section 5, we discuss the implications of our findings and conclude in Section 6.



The All-Sky Automated Survey for SuperNovae (ASAS-SN) is a ground-based photometric survey originally designed to discover bright supernovae and other transients (B. J. Shappee et al. 2014). Currently, it comprises twenty 14-cm telescopes across five stations, monitoring the entire sky nightly in the g band to a depth of $g \lesssim 18.5$ mag. Including the archival V-band data collected in 2014–2018, ASAS-SN has accumulated nearly 13 years of photometry for the longest-observed sources. To make the data accessible to the community, the ASAS-SN team launched Sky Patrol V1.0 (C. S.

[†] Here, we use the term "agent" to refer to an instance of a multimodal LLM acting as an automated annotator. Our agents are deliberately minimal, with no memory across evaluations, access to tools, or ability to plan their own actions.

Our agents are deliberately minimal: no memory, tools, or autonomous planning.

Kochanek et al. 2017), allowing users to retrieve light curves for arbitrary sky coordinates. They also released pre-computed light curves for millions of sources in both V and g bands as part of their search for variable stars (T. Jayasinghe et al. 2021; C. T. Christy et al. 2023). With the launch of Sky Patrol V2.0 (K. Hart et al. 2023), they provided access to continuously updated light curves for ∼111 million targets derived from numerous external catalogs. The primary stellar source table, which serves as the basis for this work, comprises 98 602 587 sources from the ATLAS Reference Catalog (REFCAT2, J. L. Tonry et al. 2018) with $g < 18.5$ mag for which the target contributes $> 50\%$ of the flux within a 20 arcsec radius.

The sample shrinks mainly because morphology requires a reported period, not because of aggressive quality filtering.

To assemble our sample of variable stars, we queried the Sky Patrol V2.0 database through the `pyasassn` Python client (K. Hart et al. 2023) and performed an inner join of the `master_list` table with `aavsovsx`, corresponding to the International Variable Star Index (VSX)[‡]. The join returned 502 747 ASAS-SN sources listed in VSX. Because our morphology-based analysis relies on phase-folded light curves, we retained only sources with reported periods, reducing the sample to 375 410 variable stars. For each source, we downloaded all available V- and g-band photometry (as of November 2025) and catalog metadata.

3. METHODS

In Figure 1 we show a schematic of our pipeline. First, we build an ASAS-SN light curve dataset of phase-folded light curve images and embed them with a pre-trained vision model (Section 3.1), then we establish a baseline anomaly ranking with class-conditional isolation forests trained on these embeddings (Section 3.2). Next, we iteratively refine the initial ranking through an active learning loop in which multimodal LLM agents repeatedly label the top-ranked anomaly candidates, and their labels are propagated to neighboring sources in the embedding space (Section 3.3). After the main loop, we train a logistic regression classifier on the accumulated labels, score the full unlabeled pool, and submit the top-ranked candidates to the agents for an additional round of labeling (Section 3.4). Finally, we subject all anomaly candidates flagged by the agents in the previous steps to a multi-agent consensus review (Section 3.5), producing our final catalog of anomalies and potentially interesting objects.

[‡] https://vsx.aavso.org/

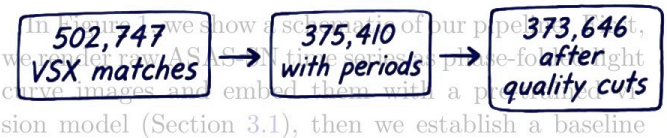
3.1. *Visual Embedding with DINOv2*

We obtained visual embeddings of the ASAS-SN light curves using the DINOv2 ViT-g/14 model (M. Oquab et al. 2023), which is a vision transformer model pre-trained on a diverse data set of approximately 142 million natural images. The self-supervised training of DINOv2 combined image-level and patch-level objectives, encouraging the model to learn semantically meaningful representations that captured both global structure and local details without requiring human-annotated labels. We deliberately chose a general-purpose vision model rather than one trained or fine-tuned on astronomical data, allowing us to test how far off-the-shelf visual representations transfer to light-curve morphology without any domain-specific adaptation.

To prepare inputs for DINOv2, we rendered each light curve as a 518×518 pixel image and let the standard preprocessing rescale it to 224×224 pixels, matching the input resolution used during the main training stage of the model. This supersampling reduced the blending of neighboring data points in densely sampled regions and preserved finer detail than rendering directly at the input resolution. Before rendering, we removed observations with bad quality flags, negative fluxes, or $\sigma_{\rm mag} > 99$ mag (corresponding to non-detections). We then phase-folded the remaining observations on the VSX period and plotted magnitude against phase over $[-0.5, +0.5]$, with the V band in blue and the g band in green. We excluded all axes, labels, and annotations so that the embeddings would capture morphology rather than spurious visual cues, but retained the magnitude range as of each plot and the period of each light curve as metadata for the subsequent analysis.

We applied quality cuts to remove sparsely observed and noise-dominated sources, requiring at least 30 observations or a peak-to-peak amplitude of 0.15 mag, yielding our final sample of 373 646 stars. We passed the light-curve images from this sample through the DINOv2 backbone and extracted their `[CLS]` tokens from the last layer, representing each light curve as a 1536-dimensional embedding vector. After extracting all embeddings, we centered them by subtracting the sample mean. This removed the common component dominating the representation, which made the embeddings more sensitive to morphological variations between sources.

Before attempting anomaly detection, we confirmed that the embeddings encode the morphological structure of the light curves by visualizing them in three dimensions with UMAP (L. McInnes et al. 2018). In Figure 2, we show the projection for the ten most common VSX variability types in our sample, which together account



We convert each clean, phase-folded light curve into a 1,536-dimensional visual description using DINOv2.

Removing axes prevents the model from learning plot furniture instead of stellar behavior.

Mean-centering suppresses the representation's common visual component and exposes subtler morphological differences.

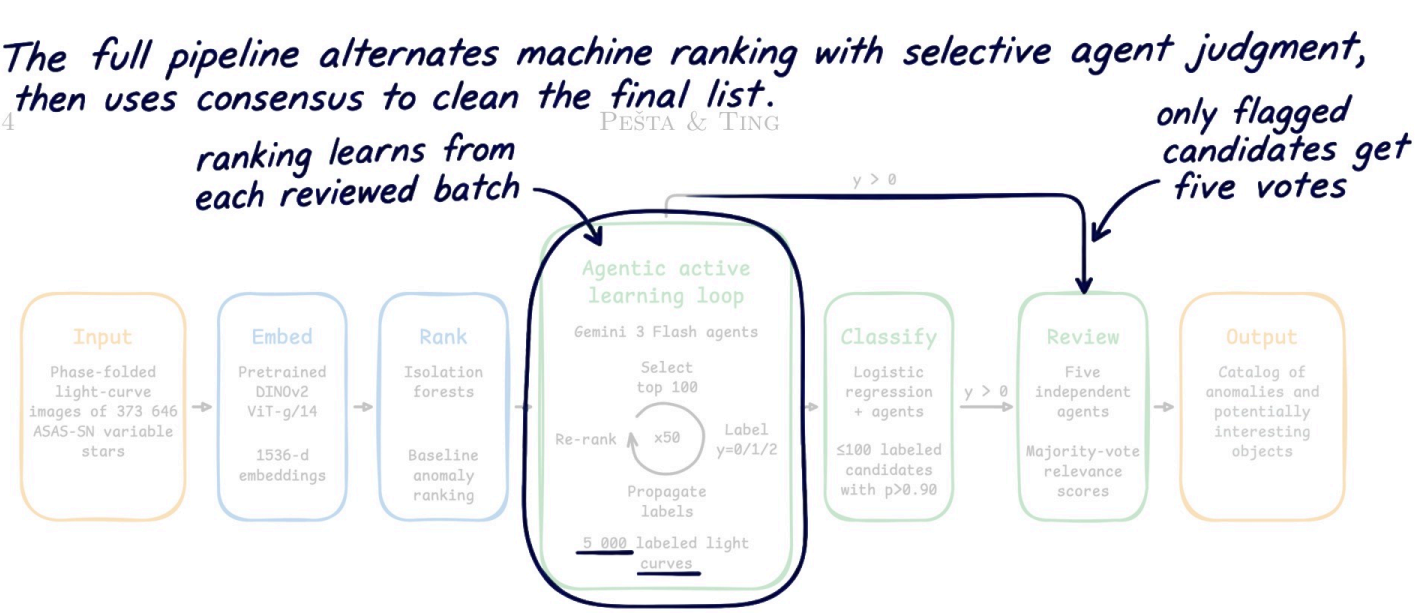


Figure 1. Schematic of our agentic active learning pipeline. Phase-folded light-curve images of 373 646 variable stars from ASAS-SN Sky Patrol V2.0 are embedded with DINOv2 ViT-g/14 and ranked with class-conditional isolation forests. Gemini 3 Flash agents then repeatedly review the 100 highest-ranked candidates over 50 iterations of an active learning loop and assign relevance scores of $y = 0$ (not interesting), $y = 1$ (potentially interesting), or $y = 2$ (anomaly). After each iteration, the scores are propagated to the neighboring sources in the embedding space, prioritizing promising candidates for the next batch. A logistic regression step (iteration 51) then trains a classifier on the accumulated labels, rescores the full pool, and selects up to 100 sources with anomaly probability $p > 0.90$ for another round of agent labeling. Finally, a multi-agent consensus review of sources with $y \geq 1$ yields a catalog of anomalies and potentially interesting objects.

for over 80% of the data. Although the embeddings were not trained on light-curve images and the class labels were not used when constructing the projection, distinct variability types occupy well-separated regions while morphologically similar classes lie adjacent.

The same pattern appears in an embedding heatmap of 10 000 randomly sampled sources from the ten most frequent classes (1 000 per class; Figure 3). The rows are grouped by class and ordered within each block by hierarchical clustering. The columns are reordered to bring correlated features together. Morphologically related classes form contiguous blocks with continuous transitions, while the sharp discontinuity between the EA and VAR blocks marks the morphological divide between regular and irregular variability. The smooth within-block gradients demonstrate that the embeddings are expressive enough to resolve the intrinsic variations within each class.

3.2. *Class-conditional Isolation Forests*

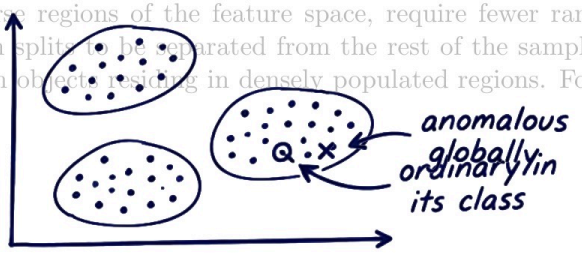
We used isolation forests (F. T. Liu et al. 2008) to establish a baseline anomaly ranking from the DINOv2 embeddings. An isolation forest is an ensemble of randomized decision trees, each of which recursively partitions the data by selecting a random feature and a random split value until every point is isolated or a maximum depth is reached. The method is based on the assumption that anomalies, being rare and occupying sparse regions of the feature space, require fewer random splits to be separated from the rest of the sample than objects residing in densely populated regions. For a single tree, the path length $h(x)$ is the number of splits along the branch connecting the root to the leaf at which source x becomes isolated. Averaging $h(x)$ for a given source over all trees in the ensemble gives the expected path length $\mathrm{E}[h(x)]$, which we converted into the normalized anomaly score

Taking the minimum cross-class percentile asks a strict question: unusual compared with every plausible class?

$$s(x, n) = 2^{-\mathrm{E}[h(x)]/c(n)}, \tag{1}$$

where n is the subsample size and $c(n)$ is the average path length in a tree of size n. This transformation bounds the score between 0 and 1, with values near unity indicating anomalies and values $\lesssim 0.5$ typical objects. Applied directly to our full sample of variable stars, a single isolation forest would tend to flag all members of rare variability classes as anomalies, even when their light curves are typical for their type, simply because those classes occupy sparsely populated regions of the embedding space by construction. To avoid this, we trained a separate isolation forest for each VSX class containing at least 1 000 members, yielding 26 class-specific models, and an additional forest for all remaining sources. Each forest consisted of 500 trees grown on random subsamples of 256 sources. Since the embeddings encode only the morphology of the light curves, we included P and Δm as additional input features.

We scored each source x in our sample against all forests, resulting in 27 separate anomaly scores for each source. We then converted these scores into percentile ranks within each forest and took the minimum across all ranks, yielding the baseline anomaly score $s^{(0)}(x)$. This cross-class minimum strategy ensures that a source



Class-conditional forests prevent an ordinary member of a rare class from being declared anomalous merely for being rare.

DINOv2 unexpectedly organizes unfamiliar light-curve plots by physical morphology, making neighborhood-based learning possible.

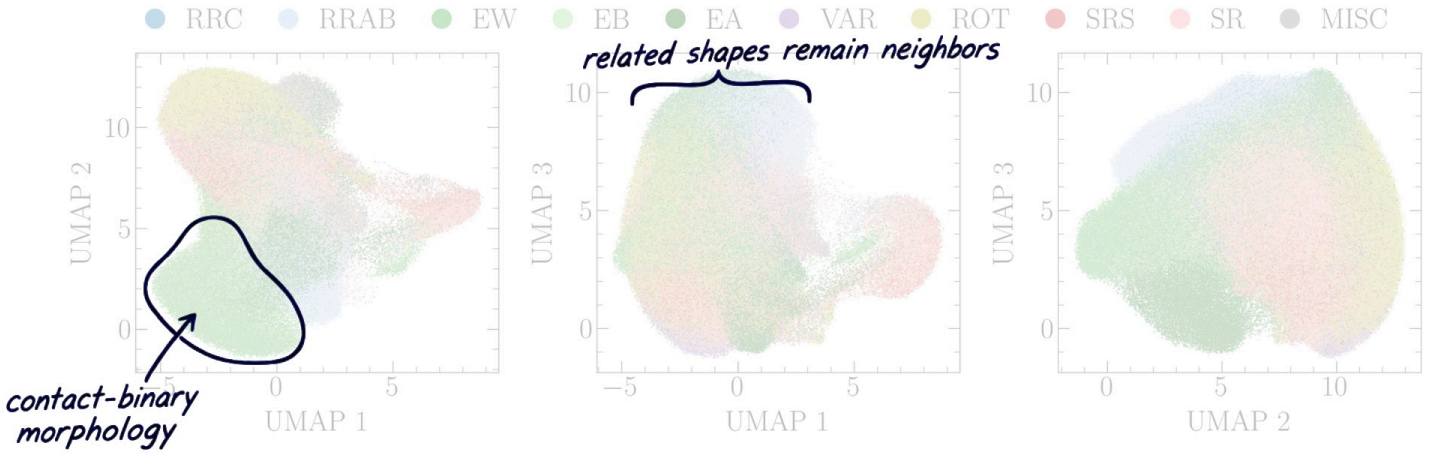


Figure 2. Three-dimensional UMAP projection of the DINOv2 embeddings for the ten most frequent VSX variability classes in our sample, spanning RR Lyrae pulsators (RRAB, RRC), eclipsing binaries (EA, EB), contact binaries (EW), semiregular variables (SR, SRS), and rotating variables (ROT), along with the unspecified (VAR) and miscellaneous (MISC) categories. Distinct variability types occupy well-separated regions and morphologically similar classes lie adjacent, even though the embeddings were not trained on light-curve images and the labels were not used in the projection.

This separation emerged without using the VSX labels to train either the embedding or the projection.

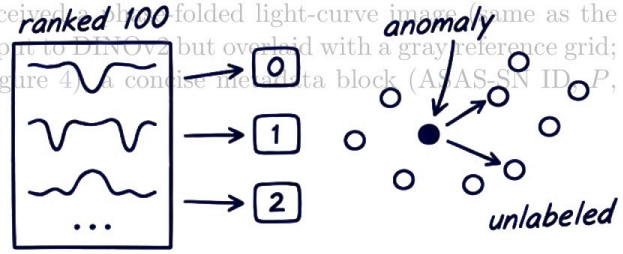
was flagged as anomalous only if it appeared unusual relative to every variability type, filtering out common objects that were assigned to the wrong class.

3.3. *Agentic Active Learning Loop*

Although isolation forests are effective at identifying outliers in high-dimensional data, they have no way of distinguishing between genuine astrophysical anomalies and data artifacts. This task has traditionally required human insight and domain knowledge, often applied in an active learning workflow for improved cost-efficiency of the labeling process (M. Lochner & B. A. Bassett 2021; V. Etsebeth et al. 2024). Here, we followed a similar approach but replaced human experts with agents powered by Gemini 3 Flash, a multimodal LLM capable of interpreting both text and images. Our motivation for doing so was twofold. First, multiple agents deployed in parallel can review anomaly candidates much faster than human experts while maintaining consistent evaluation criteria and avoiding fatigue. Second, anomaly detection provides an ideal testbed for evaluating how well the reasoning and visual capabilities of off-the-shelf models generalize to astronomy-specific tasks.

Because evaluating all sources in our sample with LLM agents would be too costly, each iteration in our active learning loop considered only the 100 unlabeled sources with the highest anomaly scores. Each light curve in the batch was evaluated independently by a single Gemini 3 Flash agent with thinking enabled, allowing the model to allocate its own reasoning effort. The agent received a phase-folded light-curve image (same as the input to DINOv2 but overlaid with a gray reference grid; Figure 4) and a concise metadata block (ASAS-SN ID, P, Δm, and VSX variability type), and a prompt instructing it to assess the light curve following the eight-step procedure shown in Figure 5.

Each iteration reviews only the top 100, so every labeling call must help reshape the next batch.



We designed the steps to mimic how human experts might approach similar tasks while mitigating the main failure modes of large language models: hallucinations and inconsistent evaluation criteria. The analysis begins with a visual inspection of the image, followed by a series of checks assessing the data quality and correctness of the period folding. The agents then estimate the amplitude of the light curve, classify the source as one of predefined variability types, flag extreme properties, and assign a relevance score of 0 (not interesting), 1 (potentially interesting), or 2 (anomaly). Finally, they audit their reasoning before producing a structured JSON output.

A few of the design choices behind this procedure are worth highlighting. We treated amplitude estimation as a separate step because our experiments showed that incorporating it into other steps reduced the accuracy of the estimates. Instead of relying on VSX labels, we had the agents classify each source and override the VSX label in case of disagreement. The assignment of the relevance score $y \in \{0, 1, 2\}$ followed a strict priority order in which the score could be elevated above zero only after the data quality and folding checks had been cleared, ensuring that artifacts could never receive a positive score. Finally, we capped long-period variables at $y \leq 1$, since large amplitudes and long periods are intrinsic to this class. We provide a condensed version of the prompt in Appendix A.

Once the agents had scored all sources in iteration t, we updated the anomaly score of each unlabeled source

Quality and folding checks come before scientific excitement; otherwise artifacts would seed entire false neighborhoods.

Agent labels propagate only to very similar neighbors, promoting anomaly-like regions while preserving exploration elsewhere.

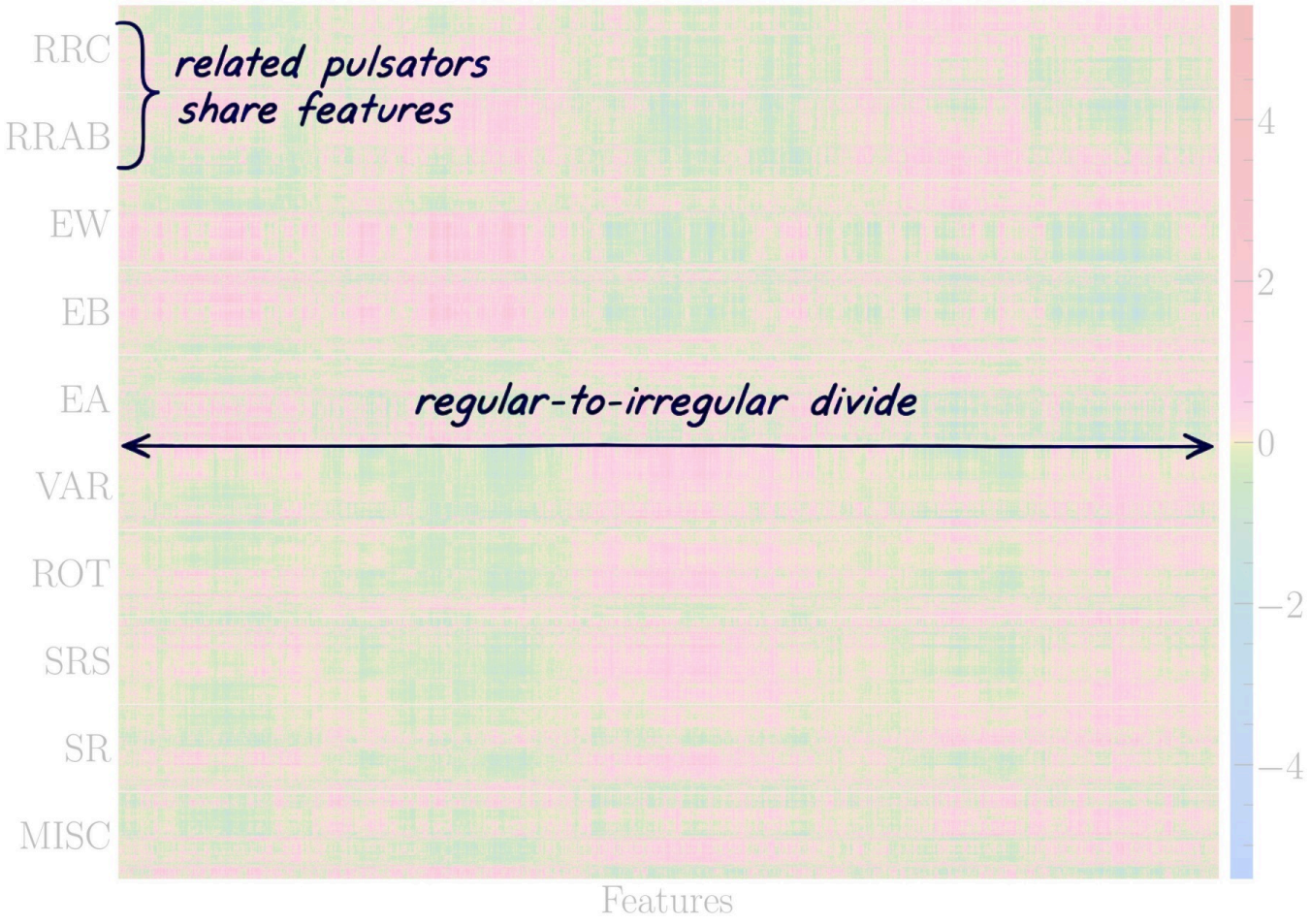


Figure 3. Heatmap of DINOv2 embeddings for 10 000 sources randomly selected from the ten most frequent VSX variability classes in our sample, with 1 000 sources per class. The color encodes feature values after centering the embeddings on the full-sample mean. The rows are grouped by class and ordered within each block by hierarchical clustering, and the feature columns are reordered to bring correlated features together. Morphologically related classes form contiguous blocks with smooth transitions, while the sharp EA–VAR boundary separates regular from irregular variability.

An anomaly neighbor forces score 1; low-scoring neighbors instead average downward.

u for iteration $t+1$ as

$$s^{(t+1)}(u) = \begin{cases} 1.0, & \text{if } y_l = 2 \text{ for any } l \in \mathcal{N}_u \neq \emptyset, \\ \langle y_l/2 \rangle_{l \in \mathcal{N}_u}, & \text{if } y_l \leq 1 \text{ for all } l \in \mathcal{N}_u \neq \emptyset, \\ s^{(0)}(u), & \text{if } \mathcal{N}_u = \emptyset, \end{cases} \tag{2}$$

where the angle brackets denote an average and $\mathcal{N}_u = \{ l \in \mathcal{L}^{(t)} : \cos\theta_{ul} > 0.90 \}$ is the neighborhood of u comprising all members of the labeled set $\mathcal{L}^{(t)}$ accumulated up to iteration t whose cosine similarity to u exceeds 0.90. This propagation mechanism promoted sources with anomaly neighbors to the top of the ranking and demoted those surrounded by low-scoring neighbors to the bottom, while sources with no labeled neighbors retained their baseline anomaly scores.

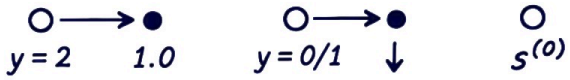
The 0.90 cosine threshold is intentionally conservative: mistaken propagation is more damaging than a missed neighbor.

To balance exploration of new regions with exploitation of known anomaly clusters, we capped the number of elevated anomaly-neighbor sources reviewed in each iteration at half the batch size. We ran the active learning loop for a total of 50 iterations, yielding 5 000 labeled sources, which then served as the training set for a logistic regression classifier.

3.5. Logistic Regression Classification

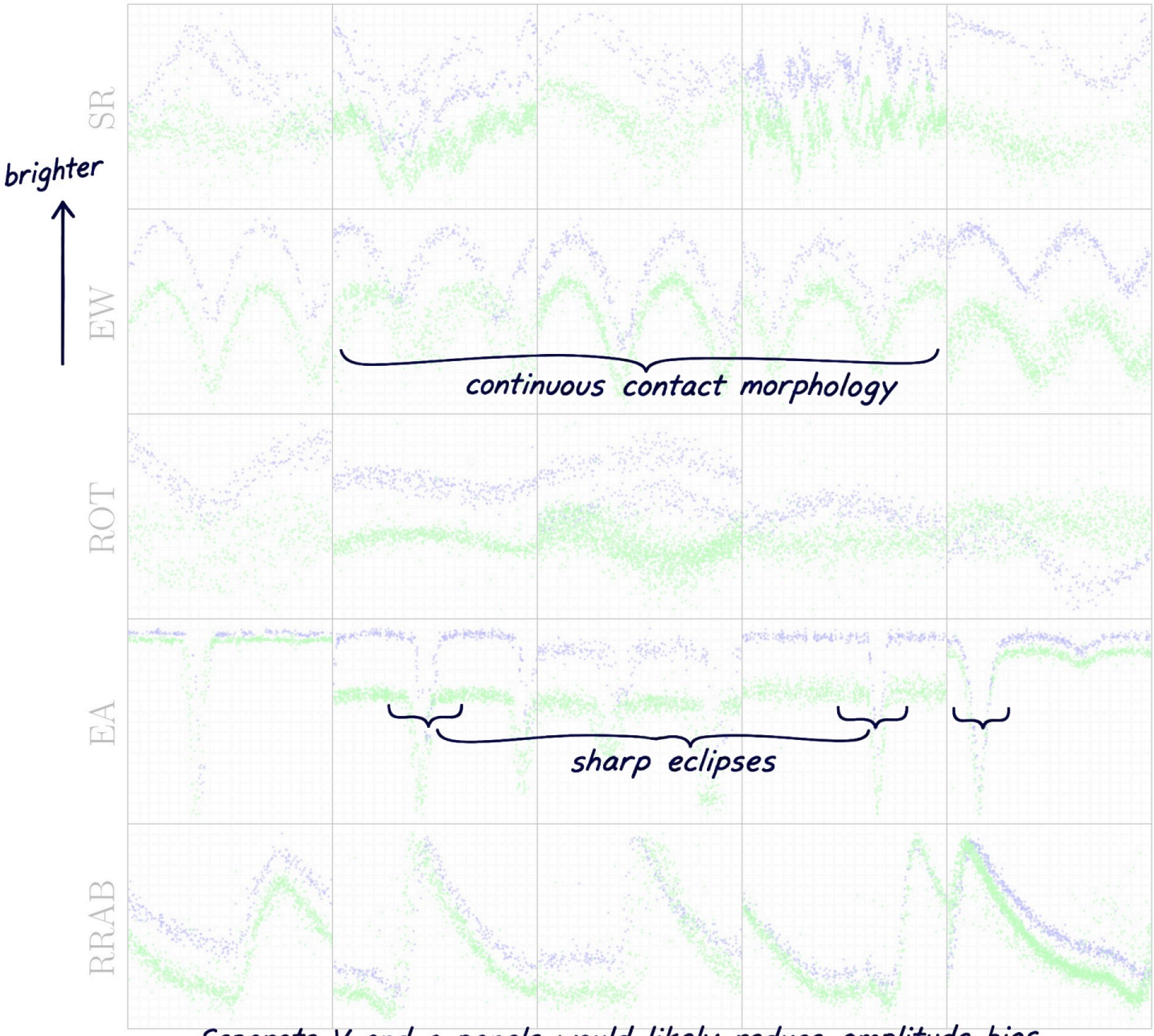
The neighbor-based propagation of Section 3.3 can only elevate sources whose similarity to an already-identified anomaly exceeds the conservative 0.90 limit, leaving genuine anomalies that fall just below this threshold out of reach. To recover them, we trained a logistic regression classifier on the relevance labels accumulated across all iterations and used it to score the entire unlabeled pool directly, without imposing a hard similarity limit.

Before training, we re-centered the embeddings on the labeled subset alone to avoid leakage from the unlabeled pool, then augmented each vector with P and Δm, and



We cap promoted neighbors at half a batch so the search does not collapse onto its first discovery.

A final logistic classifier reaches beyond the strict neighbor radius, while consensus addresses errors in individual judgments.

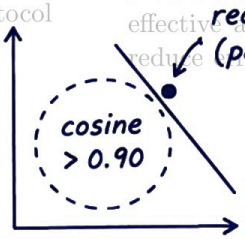


Separate V and g panels would likely reduce amplitude bias when the two filters visually overlap.

Figure 4. Examples of light-curve images [illegible] Each panel shows phase (0–1) on the horizontal axis and magnitude on the vertical axis, with brighter values toward the top. From top to bottom, the rows correspond to the five most frequent VSX classes in our sample: semiregular variables (SR), contact binaries (EW), rotating variables (ROT), eclipsing binaries (EA), and fundamental-mode RR Lyrae variables (RRAB). The V band is shown in blue, the g band in green. The gray lines indicate a 20×20 reference grid used to aid visual inspection.

standardized the features. We collapsed the three-level scale into a binary label ($y = 2$ positive, $y \in \{0, 1\}$ negative) and trained with balanced class weights to offset the class imbalance. We used the classifier to score the remaining unlabeled pool and passed up to 100 sources with anomaly probability above 0.90 to the agents for labeling, utilizing the same prompt and scoring protocol as in the main loop (Figure 5).

Logistic regression is not the initial detector; it learns the agents' accumulated definition of an anomaly.



3.5. *Multi-Agent Consensus Review*

Even when provided with detailed instructions, LLM agents can still make mistakes. For example, they may misjudge a morphological feature, misapply a class-specific threshold, or overlook a data quality issue that should disqualify a candidate. While active learning is effective at prioritizing sources for review, it does not reduce [illegible] individual agent [illegible]

Five independent reviews target reliability without paying fivefold cost on all 5,100 labels.

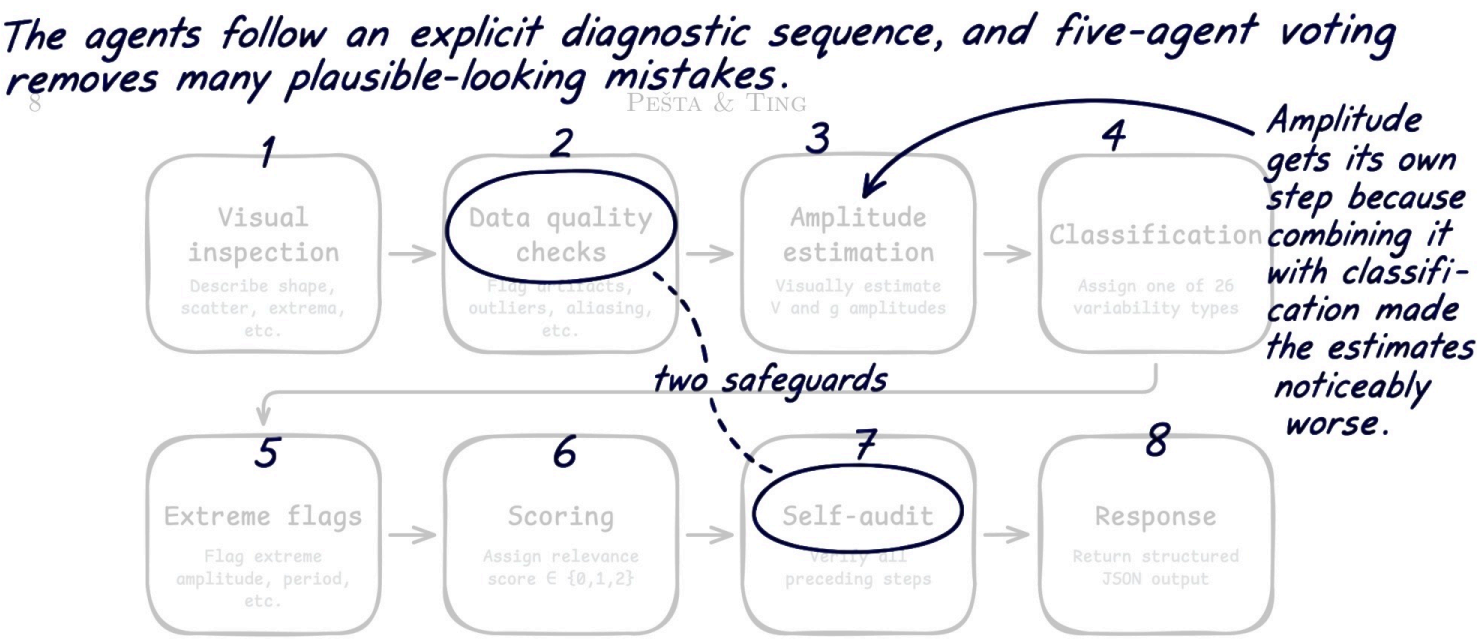


Figure 5. Schematic of the eight sequential steps that Gemini 3 Flash agents followed when evaluating anomaly candidates. The first five steps accumulate the evidence supporting the relevance score assigned in the sixth step. The self-audit then re-checks the verdict before the last step produces a structured JSON response. A condensed version of the prompt is given in Appendix A.

those errors to propagate into the anomaly candidate list. To mitigate this, we subjected all sources that received $y \in \{1, 2\}$ in the main iterative loop or the logistic regression step to a multi-agent consensus review, concentrating resources on the objects most likely to be genuine anomalies.

We submitted each candidate to five independent Gemini 3 Flash agents, each following the same eight-step prompt (Figure 5). Ties are broken toward the lower relevance class to be conservative. Since the evaluations were fully independent, the mean score across the five agents provides a continuous measure of relevance, while the variance of the scores yields a measure of confidence in the final assignment. We preserved the full reasoning chains from all five agents, ensuring that each labeling decision remains fully auditable.

Ties are resolved toward the lower relevance score; this catalog favors purity over enthusiasm.

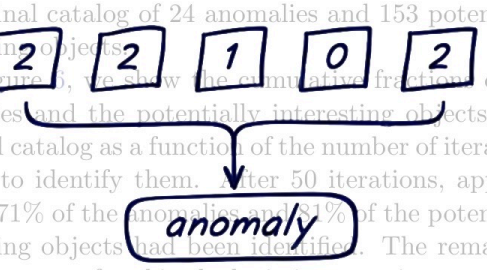
We retained every rationale, making the final votes auditable rather than opaque model outputs.

4. RESULTS

We applied the pipeline described in Section 3 to our sample of over 370 000 periodic variable stars from ASAS-SN. In Section 4.1, we report the discovery statistics and the results of the multi-agent consensus review. We present our final catalog of anomalies and potentially interesting objects in Section 4.2, before assessing the impact of adaptive re-ranking in Section 4.3.

4.1. *Discovery Statistics*

The main agentic iterative loop followed by the logistic regression step, which we collectively refer to as the single-agent stages, yielded a total of 5 100 labeled light curves. Out of these, 233 sources were assigned $y = 1$ (potentially interesting) and 43 were assigned $y = 2$ (anomaly). We subjected all 276 sources to a multi-agent consensus review, where each candidate was evaluated by five independent Gemini 3 Flash agents. Of the 43 sources initially flagged as anomalies, only 20 retained the classification, while 9 were downgraded to potentially interesting and 14 were reclassified as not interesting. Conversely, 4 sources originally rated as potentially interesting were promoted to anomaly status after the consensus review, while 85 were demoted to not interesting. We show the full label-transition matrix in Table 1. Overall, the consensus review demoted 99 of the 276 flagged sources to not interesting, resulting in our final catalog of 24 anomalies and 153 potentially interesting objects.



In Figure 6, we show the cumulative fractions of the anomalies and the potentially interesting objects from our final catalog as a function of the number of iterations it took to identify them. After 50 iterations, approximately 71% of the anomalies and 81% of the potentially interesting objects had been identified. The remaining sources were surfaced in the logistic regression step (iteration 51), which contributed 7 anomalies and 29 potentially interesting objects, extending the search beyond the reach of similarity-based label propagation.

The cumulative yield curves in Figure 7 show the fractions of all sources labeled up to a given iteration that ended up in our final catalog as anomalies and potentially interesting objects. The anomaly curve remains nearly flat at roughly 0.4% throughout iterations 2–50, while the yield of the potentially interesting objects rises steadily from approximately 1% to 2.5% between iter-

Consensus removes 99 weak positives, while the logistic-regression round supplies a conspicuous final jump in discoveries.

Table 1. Label transitions between the single-agent stages (rows) and the multi-agent consensus review (columns). The review demoted 99 of the 276 positive single-agent labels to not interesting, yielding our final catalog of 24 anomalies and 153 potentially interesting objects.

	Consensus review			
Single-agent	Anomaly	Potentially interesting	Not interesting	Total
Anomaly	20	9	14	43
Potentially interesting	4	144	85	233
Total	24	153	99	276

99 demotions

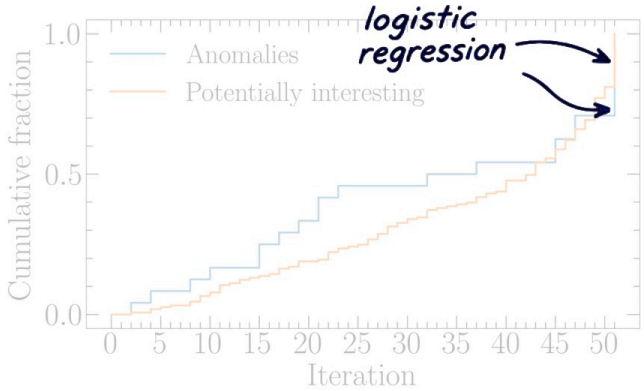


Figure 6. Cumulative fractions of the anomalies and the potentially interesting objects from our final catalog as a function of the number of iterations needed to identify them. The jump at iteration 51 corresponds to the logistic regression step, which contributed 29% of the anomalies and 19% of the potentially interesting objects to the catalog.

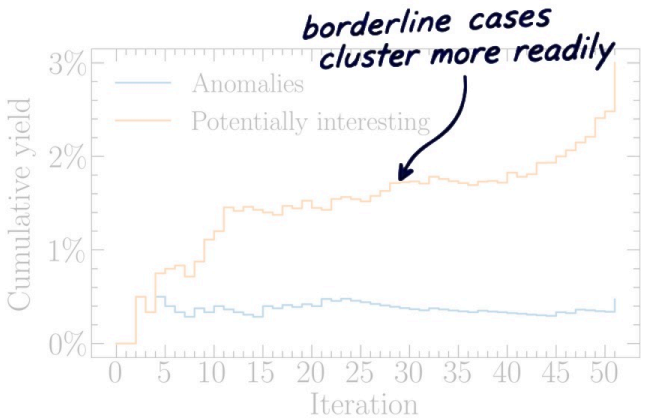


Figure 7. Cumulative yield, computed as the fraction of all sources labeled up to a given iteration that ended up in our final catalog, shown separately for anomalies and potentially interesting objects. The anomaly curve stays nearly flat at approximately 0.4% throughout iterations 2–50, while the cumulative yield of the potentially interesting objects rises steadily from about 1% to roughly 2.5% between iterations 10 and 50, reflecting the different efficiency with which the active learning loop enriches successive batches in the two cases. The jump in both curves at iteration 51 corresponds to the logistic regression step.

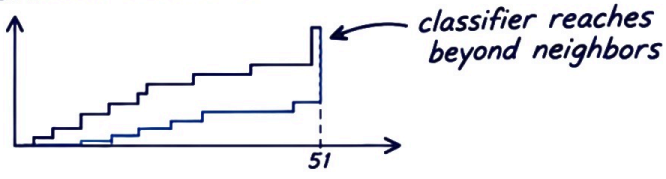
ations 10 and 50. The reason is that in the latter case both similarity-based elevation and demotion of uninteresting objects contribute comparably to the enrichment of each successive batch, whereas for anomalies, which are naturally scarce and isolated, elevation is much less effective. Despite this, both curves show a jump at iteration 51, reflecting the increased yield of the logistic regression step.

Table 2 breaks the 276 flagged sources down by majority-vote variability class. EA-type eclipsing binaries, contact binaries, and RRab variables (fundamental-mode RR Lyrae) together account for 87.5% of the anomalies, with Type II Cepheids and a single dwarf nova making up the rest. The potentially interesting objects follow a similar distribution, with the same top three classes comprising 86.9% of them. The remaining sources span many classes, including EB-type eclipsing binaries, rotating variables, and semiregular variables. This long tail most likely reflects the larger sample size of potentially interesting objects rather than any systematic difference between the two relevance categories.

A low anomaly yield is expected: true anomalies are scarce and often isolated from one another.

The per-class demotion rates (DRs) in Table 2 show the fraction of each variability class reclassified as not interesting during the consensus review. Among the three most frequent classes, the DRs range from 0.24 to 0.38, with EA-type eclipsing binaries exhibiting the lowest rate. Their sharp V-shaped eclipses against flat out-of-eclipse baselines likely made the light curves straightforward to interpret, resulting in the low DR. In contrast, EB-type eclipsing binaries, rotating variables, and semiregular variables were all demoted at rates exceeding 0.6. Most EB-type variables were misclassified as contact binaries, which led to their periods and amplitudes being evaluated against the tighter ranges of that class, making otherwise typical light curves appear anomalous. Meanwhile, the [illegible] and rotating and semiregular variables [illegible] difficulty for humans to reliably estimate amplitudes and identify data quality

Potentially interesting objects benefit more from neighborhood enrichment because borderline morphologies form broader clusters.



The strongest detections are deep eclipsing systems, high-amplitude contact binaries and pulsators, plus one decades-long nova outburst.

issues, causing them to flag ordinary variables as anomalies. These failure modes can also be seen in an n-gram analysis of the rationales from the consensus review, where the vocabulary for the demoted sources splits between misflagged class-standard objects and overlooked data quality issues (Appendix B).

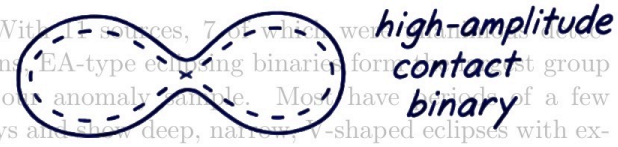
4.2. *Anomalies*

In Table 3, we list all 24 anomalies identified in the multi-agent review, together with their periods, VSX class labels, majority-vote classifications, mean per-filter amplitudes, and mean relevance scores from the consensus review. We show their phase-folded light curves in Figures 8 and 9. By agent classification, the anomaly sample spans 11 EA-type eclipsing binaries, 7 contact binaries, 3 RRab variables, 2 Type II Cepheids, and a single dwarf nova. Of these, 9 received unanimous anomaly scores from all five agents, making them the highest-confidence detections in the sample: Z Crt, SW Phe, RU CMa, NSV 1789, AG Pav, Y Leo, V0441 Oph, HM Pup, and CSS_J085817.6−075719.

4.2.1. *Data Quality and Amplitude Checks*

We manually inspected the light curves of all 24 anomalies for data artifacts and compared the agent-estimated amplitudes with our own. Several light curves contain sparse outliers, but in most cases these remain isolated enough from the main signal that the agents did not absorb them into their amplitude estimates. The exception is BH Aps, where three out of five agents confused the outliers with the eclipse floor, inflating the mean g-band amplitude to 4.72 ± 1.07 mag compared to our estimate of 3.5 mag. In all remaining cases, the agent-estimated g-band amplitudes agree with ours to within 15%. The agreement is poorer in the V band, where the agents overestimated the eclipse depths of several EA-type binaries with visually overlapping bands (e.g., Z Crt, SW Phe), apparently extrapolating the V-band points toward the deeper g-band minimum. The overestimation is absent when the two bands are well separated or only marginally overlap, supporting this interpretation.

4.2.2. *Eclipsing Binaries*



With 11 sources, 7 of which were flagged by multiple agents, EA-type eclipsing binaries form the largest group in our anomaly sample. Most have periods of a few days and show deep, narrow, V-shaped eclipses with extreme g-band depths of 4.02–4.82 mag (97–99% flux decrease) and no well-defined secondary minima, pointing to high-inclination configurations in which a hot primary is occulted by a larger but much cooler secondary. A. Liakos et al. (2022) confirm this configuration for HM Pup, identifying it as a semidetached binary observed at inclination 89.7 ± 0.3 deg with an A6V primary and a larger K8IV/III secondary. Similarly, G. Giuricin et al. (1980) found Y Leo to be a semidetached binary consisting of an A2 primary and a larger K-type secondary, observed at inclination 85.3 ± 1.2 deg. In addition, Z Crt, SW Phe, and V0441 Oph all have primaries of spectral type A according to VSX, consistent with this picture.

Several deep eclipsers fit a hot compact primary hidden by a larger, cooler companion.



The two sources that depart from this picture are BH Aps and ASAS J174600−2321.3. The reported eclipse depth of BH Aps is about 3.5 mag, potentially placing it within the normal range for EA systems and casting doubt on its anomaly status. This uncertainty is also reflected in its mean relevance score of 1.4, which is among lowest in the sample. ASAS J174600−2321.3, on the other hand, has a long period of 1011.5 d and shows a wide eclipse profile with agent-estimated depths of $A_V = 3.76 \pm 0.15$ mag and $A_g = 3.03 \pm 0.23$ mag. S. Hümmerich et al. (2015) identified it as an eclipsing symbiotic binary, in which a white dwarf primary undergoing a slow nova outburst is periodically occulted by a late M giant companion. F.-J. Hambsch et al. (2015) analyzed the system further and found a slight decrease in the mean brightness, suggesting that the eruption had begun to subside. Nearly a decade later, our data show that the white dwarf is still in outburst.

Beyond the deep eclipses, most light curves show out-of-eclipse scatter at the level of $\gtrsim$0.5 mag, far above the expected photometric noise. The scatter is one-sided, extending toward fainter magnitudes, which points to saturation-induced bias rather than intrinsic variability. Indeed, the out-of-eclipse baselines of these sources lie at $g \approx 10$–11.5 mag, well into the saturation regime of the survey, which sets in at $g \approx 12.5$ mag (K. Hart et al. 2023). However, this does not undermine the extreme eclipse depths, since a baseline biased toward fainter magnitudes can only make the eclipses appear shallower, not deeper.

Saturation broadens many bright baselines downward, so it can only make these extreme eclipse depths look shallower.

4.2.3. *Contact Binaries*

The seven contact binaries, including the unanimously voted CSS_J085817.6−075719, all show the smooth double-wave morphology characteristic of the class. Their periods of 0.27–0.46 d fall well within the typical range, but $A_V = 0.85$–1.30 mag and $A_g = 1.11$–1.30 mag place them in the high-amplitude tail of the distribution. The amplitude dependence analysis in M. Pešta & O. Pejcha (2023) indicates that these systems are most likely high-inclination, near-equal-mass binaries in deep contact (fill-out factor ≥ 0.5). The combination of the short periods and large fill-out factors suggests that some of these systems may be close to filling their outer

ASAS J174600−2321.3 shows that "periodic variable" can conceal a symbiotic nova still evolving over decades.

Agent reliability depends strongly on morphology: crisp detached eclipses are easier than noisy or easily confused classes.

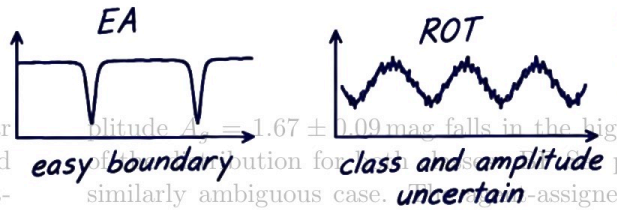
Table 2. Consensus relevance labels and demotion rates by majority-vote variability class.

Majority-Vote Class	Anomalies	Potentially Interesting	Not Interesting	Total	DR
Eclipsing binary (EA)	11	60	22	93	0.24
Contact binary	7	49	35	91	0.38
RR Lyrae (RRab)	3	24	10	37	0.27
Eclipsing binary (EB)	0	9	16	25	0.64
Rotating variable	0	2	6	8	0.75
Semiregular variable	0	2	4	6	0.67
RR Lyrae (RRc)	0	3	2	5	0.40
Type II Cepheid	2	2	0	4	0.00
δ Scuti	0	1	1	2	0.50
Classical Cepheid	0	1	0	1	0.00
RV Tauri	0	0	1	1	1.00
Contact binary/Eclipsing binary (EB)	0	0	1	1	1.00
Dwarf nova	1	0	0	1	0.00
Unknown	0	0	1	1	1.00
Total	24	153	99	276	0.36

lowest among common classes

main confusion zone

NOTE—Sample comprises 276 candidates initially flagged as "Anomaly" or "Potentially Interesting" in the single-agent stages. *DR* (demotion rate) is the fraction of each class demoted to "Not Interesting" in consensus review. *Majority-Vote Class* is assigned by majority vote of five agents in the consensus review. Slash (/) denotes a tie in the majority vote. Parenthetical labels denote a subtype, if any. Some agent-defined classes group multiple VSX labels (e.g., Type II Cepheid groups CW, CWA, CWB). See our GitHub repository for the full agent-to-VSX class mapping.



Class-dependent failure rates matter whenever an LLM applies numerical thresholds after visual classification.

critical Roche lobes, at which point mass and angular momentum loss through the L2 Lagrange point would drive rapid merger, making them particularly interesting targets for follow up.

4.2.4. *Pulsators*

The five pulsators consist of three RRab variables and two Type II Cepheids as classified by the agents. The RRab systems display the asymmetric sawtooth profile typical of the class, but their faint magnitudes (16–18 mag) introduce substantial photometric scatter in the folded light curves, possibly compounded by Blazhko modulation. This could have inflated the agent-estimated amplitudes of $A_V = 1.43$–1.60 mag and $A_g = 1.47$–1.72 mag, but even the lower bounds on these estimates (Table 3) still exceed or fall just below the 1.3 mag threshold we adopted for RRab variables, placing the systems at the high-amplitude end of the distribution.

The agents classified NSV 1789 as a Type II Cepheid, matching its VSX label. However, the long period of 109.1 d is more consistent with that of a classical Cepheid, which is also supported by the literature (e.g. M. A. T. Groenewegen & J. Lub 2023; T. R. Carson & R. B. Stothers 1984). At this period, the high amplitude $A_g = 1.67 \pm 0.09$ mag falls in the high-end tail of the amplitude distribution for classical Cepheids. OGLE-BLG-CEP-001 presents a similarly ambiguous case. The agent-assigned class of Type II Cepheid agrees with A. M. Yacob et al. (2022), while VSX listed the star as AHB1 (above horizontal branch variable of subtype 1) at the time of our data retrieval. The VSX label has since been updated to ACEP, corresponding to an anomalous Cepheid pulsating in the fundamental mode. The distinction between Type II and anomalous Cepheids is not important here, since the combination of the short period $P = 1.17$ d and high amplitude $A_g = 1.38 \pm 0.16$ mag makes BF Ser unusual under either classification.

4.2.5. *Nova-like Variable*

The agents classified RW Tri as a dwarf nova in quiescence, but the steady baseline near 13 mag is too bright for this class. The VSX catalog instead lists RW Tri as EA/WD+NL with spectral type pec(cont+e)+M0V, corresponding to an eclipsing binary with a white dwarf primary, red dwarf secondary, and nova-like variability. Most likely, the agents conflated the two classes due to the absence of a nova-like class description in the prompt. Despite the physical differences, their typical amplitude ranges overlap, justifying the extreme

EB systems were often mistaken for contact binaries, then judged against the wrong amplitude and period limits.

Noise in rotating and semiregular variables encouraged both amplitude overestimation and missed quality problems.

The 24-object catalog is ordered by consensus confidence, not by physical extremeness or discovery importance.

Table 3. List of the 24 anomalies identified in the multi-agent consensus review.

Rank	Name	P (d)	VSX Class	Agent Class	A_V (mag)	A_g (mag)	$\bar{y}$
1	Z Crt	3.05	EA/SD	Eclipsing binary (EA)	3.96 ± 0.14	4.07 ± 0.09	2.0
2	SW Phe	2.55	EA/SD	Eclipsing binary (EA)	4.20 ± 0.13	4.38 ± 0.06	2.0
3	RU CMa	1.98	EA/SD	Eclipsing binary (EA)	3.55 ± 0.46	4.23 ± 0.21	2.0
4	NSV 1789†	109.1	CWA	Type II Cepheid	1.14 ± 0.14	1.67 ± 0.09	2.0
5	AG Pav	1.96	EA	Eclipsing binary (EA)	3.44 ± 0.20	4.16 ± 0.09	2.0
6	Y Leo†	1.69	EA/SD+DSCT	Eclipsing binary (EA)	4.82 ± 0.24	4.82 ± 0.21	2.0
7	V0441 Oph	3.06	EA/SD	Eclipsing binary (EA)	4.21 ± 0.12	4.33 ± 0.12	2.0
8	HM Pup†	2.59	EA+DSCT	Eclipsing binary (EA)	4.18 ± 0.10	4.34 ± 0.23	2.0
9	CSS_J085817.6−075719	0.30	EW	Contact binary	1.30 ± 0.16	1.30 ± 0.09	2.0
10	ASASSN-V J022324.79−275944.7	0.27	EW	Contact binary	1.09 ± 0.15	1.13 ± 0.12	1.8
11	CSS_J163724.5+181022	0.47	RRAB	RR Lyrae (RRab)	1.60 ± 0.21	1.72 ± 0.20	1.8
12	PS1-3PI J172130.15+035957.1	0.54	RRAB	RR Lyrae (RRab)	1.43 ± 0.16	1.53 ± 0.14	1.8
13	BF Ser†	1.17	AHB1	Type II Cepheid	1.14 ± 0.10	1.38 ± 0.16	1.6
14	SSS_J062839.1−352411	0.27	EW	Contact binary	0.94 ± 0.08	1.12 ± 0.15	1.6
15	RW Tri†	0.23	EA/WD+NL	Dwarf nova	2.78 ± 0.14	2.93 ± 0.16	1.6
16	WISE J124249.8−755621	0.29	EW	Contact binary	1.20 ± 0.09	1.13 ± 0.09	1.6
17	SSS_J221404.0−395131	0.30	EW	Contact binary	0.99 ± 0.28	1.13 ± 0.19	1.6
18	LINEAR 12081294	0.46	EW	Contact binary	1.17 ± 0.14	1.11 ± 0.18	1.6
19	PS1-3PI J191804.23−183644.3	0.50	RRAB	RR Lyrae (RRab)	1.43 ± 0.28	1.47 ± 0.26	1.6
20	ASAS J174600−2321.3†	1011.5	NC+EA+SR	Eclipsing binary (EA)	3.76 ± 0.15	3.03 ± 0.23	1.6
21	TW Pup	2.89	EA	Eclipsing binary (EA)	4.27 ± 0.09	4.33 ± 0.07	1.6
22	RX CMa	2.07	EA/SD	Eclipsing binary (EA)	3.51 ± 0.53	4.02 ± 0.04	1.6
23	BH Aps	3.65	EA/SD	Eclipsing binary (EA)	4.69 ± 1.04	4.72 ± 1.07	1.4
24	CSS_J223902.0+232058	0.28	EW	Contact binary	0.85 ± 0.11	1.13 ± 0.26	1.4

unanimous five-agent anomalies

NOTE—*Rank* is set by decreasing mean relevance score $\bar{y}$, with ties broken by the minimum score across the five agents in the consensus review. *VSX Class* is taken from the International Variable Star Index; slash (/) marks a subtype, plus (+) a combination of variability types, and colon (:) an uncertain classification. *Agent Class* is the consensus variability type adopted in the multi-agent review. P is the VSX-reported period in days. A_V and A_g are the per-filter amplitudes (in magnitudes), reported as mean ± standard deviation across the agents. Dagger (†) marks objects previously studied in the literature, with references given in Section 4.2.7.

exceptionally long-period system

amplitude flag even in the nova-like case. With an eclipse depth of about 2.8 mag, RW Tri represents one of the deepest eclipsing nova-like systems (D. Kjurkchieva et al. 2015), and as such it has been analyzed extensively in the literature (e.g., D. Boyd 2023; G. Subebaatar et al. 2018). Taken together, the agents interpreted the streaks as data quality issues, resulting in a majority-vote score of 0. The ambiguous case is the eclipsing binary UU Oph with an agent-estimated eclipse depth $A_g = 2.59 \pm 1.24$ mag and three sparse points extending it to ≈4.8 mag that four agents interpreted as outliers. Without additional photometry, it is difficult to assess whether the demotion was justified.

A lower mean score does not mean uninteresting; it often records disagreement about data quality.

4.2.6. *Demoted Anomalies and Potentially Interesting Objects*

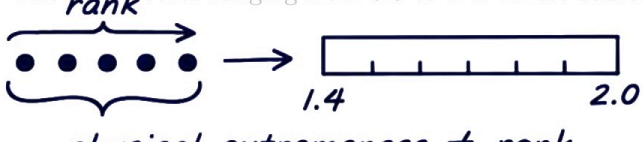
We also inspected the 23 sources that were initially flagged as anomalies and then demoted during the consensus review. We found most demotions justified, with two exceptions and one ambiguous case. CSS_J123713.5−114008 is an RRab variable misclassified as EW in VSX, which led one of the agents to flag it

BH Aps is the cautionary endpoint: sparse outliers inflated several agents' eclipse-depth estimates.

outlier-sensitive estimate

for aliasing, preventing a majority anomaly vote despite its high amplitude $A_g = 1.58 \pm 0.17$ mag. AQ Ind is an eclipsing binary with an extremely deep primary eclipse ($A_g = 4.34 \pm 0.22$ mag) that, due to the arbitrary phase zero-point, appeared as two sparse streaks at the edges

Beyond the anomalies, the consensus review also flagged 153 potentially interesting sources, with mean relevance scores ranging from 0.6 to 1.4. These sources



physical extremeness ≠ rank

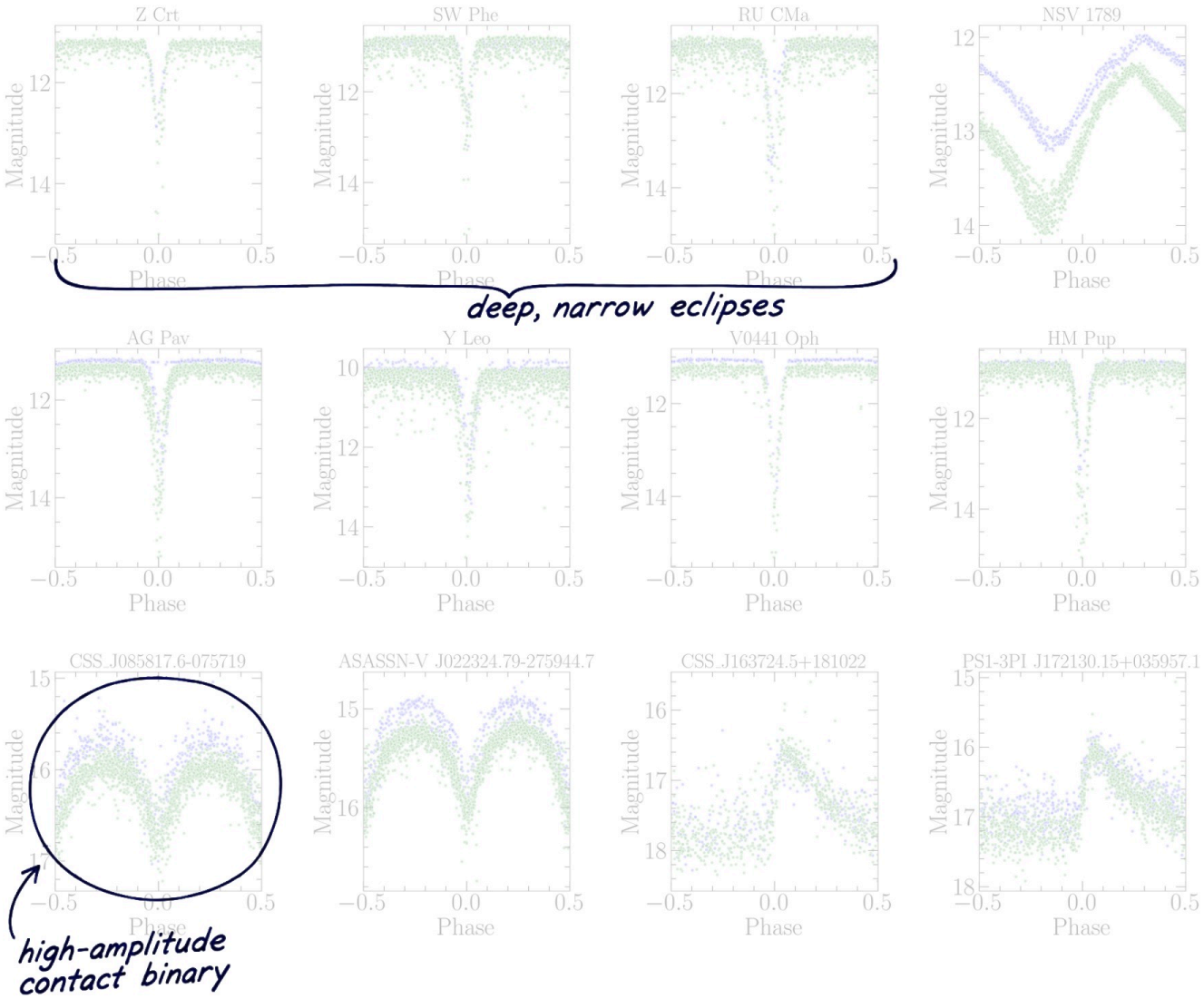


Figure 8. Phase-folded light curves of the anomalies ranked 1–12 in Table 3, with each panel labeled by the source name. The first nine sources were unanimously voted anomalies by all five agents in the consensus review. The V-band is shown in blue, the g-band in green.

show borderline behavior such as near-boundary amplitudes or periods, mild modulation, or possible secondary periodicities, none of which were pronounced enough to secure a majority anomaly vote. Still, the five highest-ranked potentially interesting objects were flagged as anomalous by two out of five agents, making them worth revisiting. We list the five potentially interesting sources together with the three demoted anomalies in Table 4 and show all eight light curves in Figure 10.

4.2.7. *New discoveries*

Of the 24 anomalies identified by the pipeline, 6 have been previously studied in the literature for their unusual properties (NSV 1789: M. F. Wils & J. Lub 2023; J. C. Pigott et al. 2009; V0441 Oph: A. Pop et al. 2011; A. Pop et al. 2011), HM Pup (A. Liakos et al. 2022; D. J. W. Moriarty et al. 2013), BF Ser (J. Ashbrook 1950; E. G. Schmidt et al. 2003), RW Tri (N. F. Vojkhanskaya 1984; J. Smak 2019), and ASAS J174600−2321.3 (S. Hümmerich et al. 2015; F.-J. Hambsch et al. 2015), with NSV 1789, Y Leo, and HM Pup receiving unanimous anomaly scores from all five agents. For the remaining 18 sources, prior work is limited to their identification as variable stars and the determination of their periods and ephemerides, making them new discoveries in the context of anomaly detection, though spectroscopic follow-up is needed to confirm their nature. We make the full catalog of all 24 anomalies and 153 potentially interesting objects available in our online data release.

The other 18 are new as anomalies, although spectroscopy is still needed to establish their physical nature.

~4-mag eclipse

contact binary

The six literature-known systems provide an independent sanity check because agents saw no names or coordinates.

Adaptive re-ranking surfaces anomalies missed by the fixed initial ranking within the labeling budget.

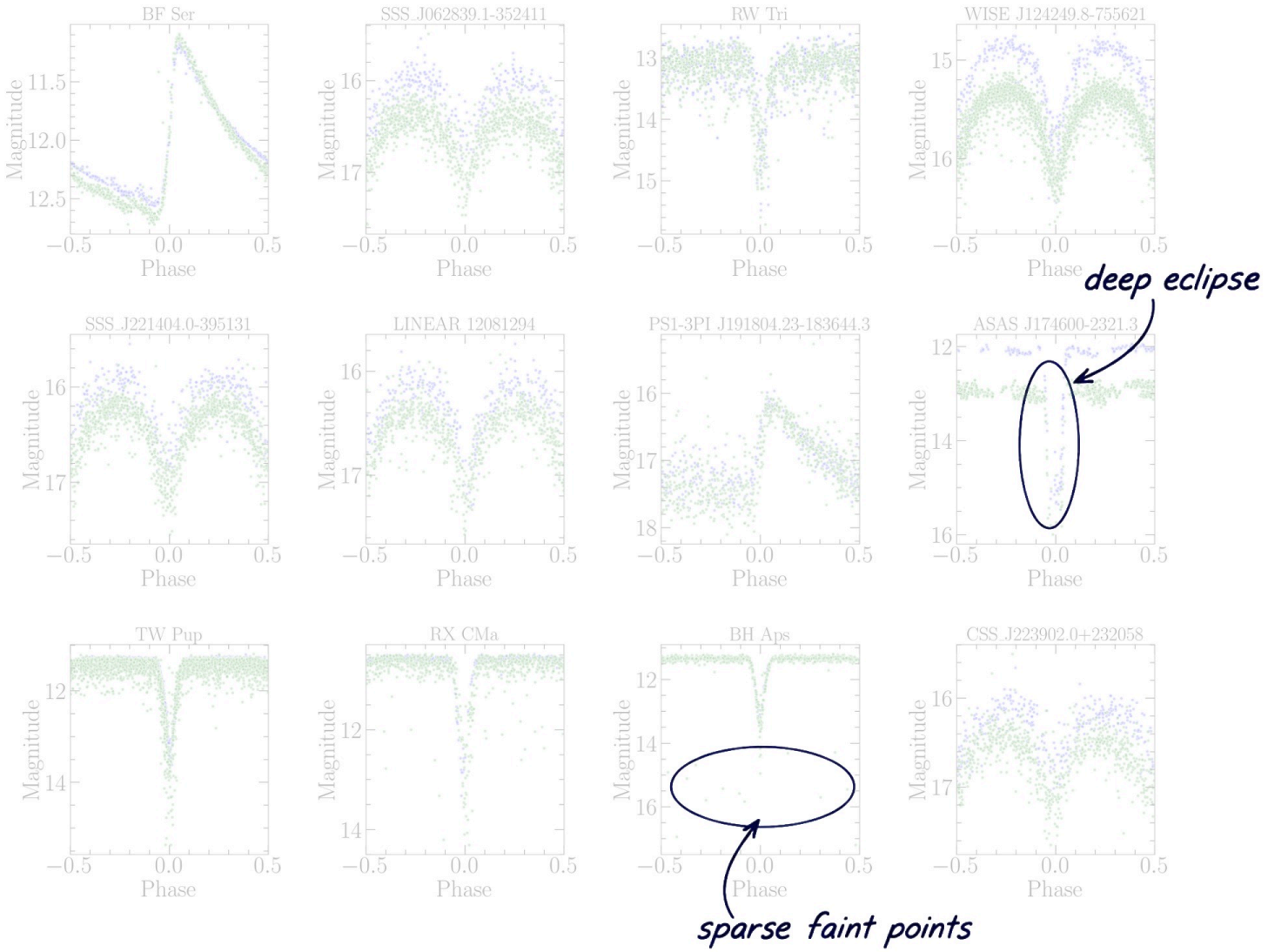


Figure 9. Same as Figure 8, for the anomalies ranked 13–24 in Table 3.

4.3. *Adaptive Re-ranking*

The rank trajectories in Figure 11 provide direct evidence of the efficiency of our active learning loop, showing the dramatic improvements achieved by the adaptive updates of the ranking as the iterations proceed. Under the initial isolation-forest ranking, only 7 of the unanimous anomalies (78%) and 10 of the 24 anomalies identified in total (42%) would have fallen within our labeling budget of 5 100 sources. Across all 24 anomalies, the most extreme case is CSS_J163724.5+181022, which started near rank 3.5×10^5 and was surfaced only at iteration 51 by the logistic regression classifier trained on the labels accumulated throughout the main loop. The effect is even stronger for potentially interesting objects, where only 43 of the 153 sources from our final catalog (28%) would have been labeled under the fixed initial ranking.

CSS J163724.5+181022 began near rank 350,000; label-trained logistic regression surfaced it at iteration 51.

At a 5,100-source budget, the fixed initial ranking would recover only 10 of the final 24 anomalies (42%).

5. DISCUSSION

Utilizing pre-trained visual embeddings and off-the-shelf LLM agents, our agentic active learning pipeline identified 24 anomalies, 18 of them newly reported, and 153 potentially interesting objects. We discuss the effectiveness of the visual embeddings in Section 5.1, assess the reliability of the LLM judges in Section 5.2, examine the impact of the active learning loop in Section 5.3, consider the scalability of the pipeline in Section 5.4, and outline its limitations in Section 5.5.

5.1. *Visual Embeddings*

Our results show that vision foundation models trained on natural images can encode light curve images despite the profound domain shift from everyday scenes to scatter plots of magnitude versus phase. Without fine-tuning or catalog-label supervision, the DINOv2

Figure 10 compares five potentially interesting sources with three demoted cases warranting further investigation.

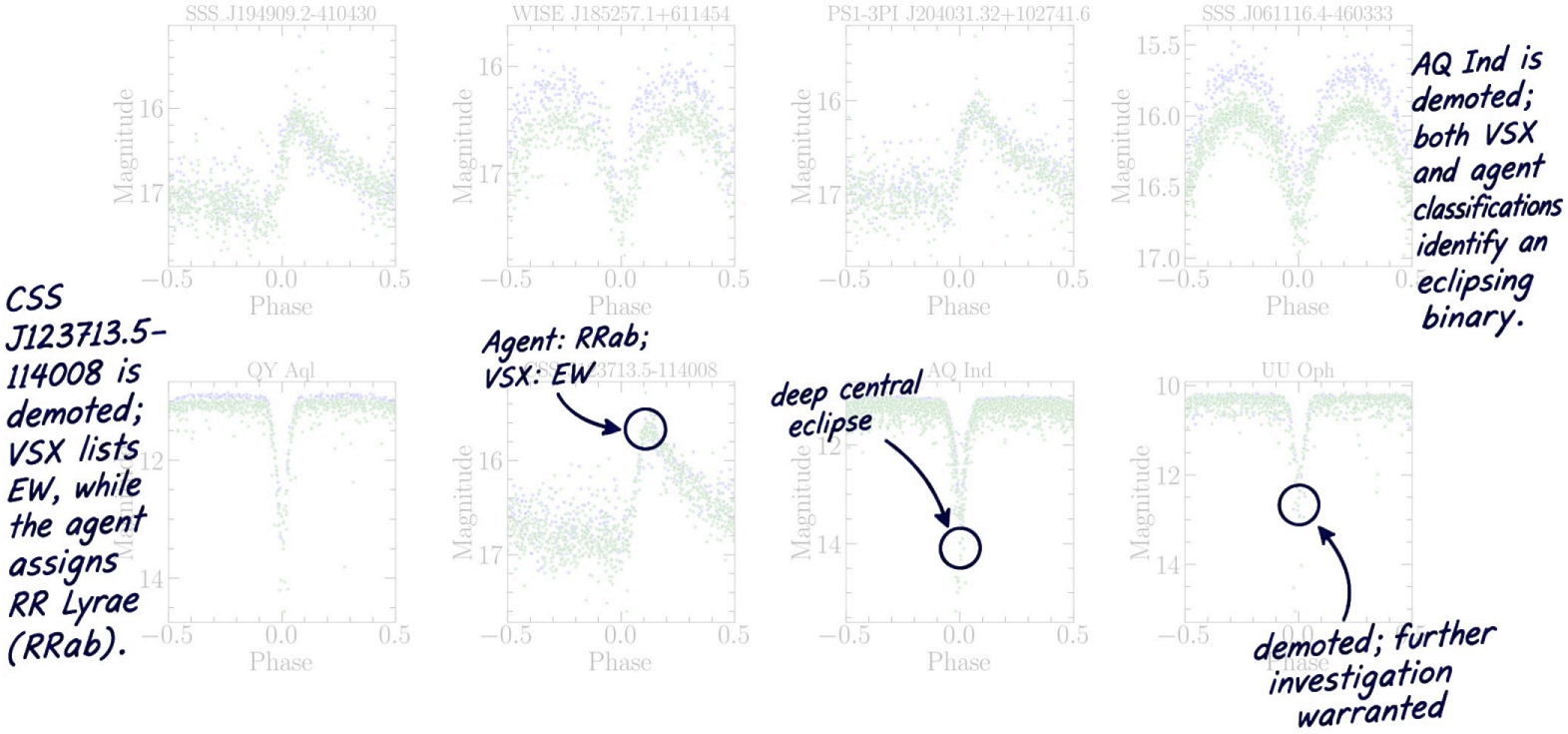


Figure 10. Phase-folded light curves of the five highest-ranked potentially interesting sources from the multi-agent consensus review, followed by three demoted sources warranting further investigation: CSS_J123713.5−114008, AQ Ind, and UU Oph. Each panel is labeled by source name. The V-band is shown in blue, the g-band in green.

UU Oph is demoted; VSX lists EA/SD, while the agent assigns eclipsing binary (EA).

Table 4. Five highest-ranked potentially interesting objects from the multi-agent consensus review and three demoted sources warranting further investigation.

Rank	Name	P (d)	VSX Class	Agent Class	A_V (mag)	A_g (mag)	$\bar{y}$
			Potentially interesting				
25	SSS_J194909.2−410430	0.60	RRAB	RR Lyrae (RRab)	1.39 ± 0.14	1.41 ± 0.14	1.4
26	WISE J185257.1+611454	0.34	EW	Contact binary	0.99 ± 0.21	1.16 ± 0.21	1.4
27	PS1-3PI J204031.32+102741.6	0.55	RRAB	RR Lyrae (RRab)	1.37 ± 0.11	1.42 ± 0.11	1.4
28	SSS_J061116.4−460333	0.34	EW	Contact binary	0.87 ± 0.11	1.04 ± 0.10	1.4
29	QY Aql	7.23	EA/DS:	Eclipsing binary (EA)	3.42 ± 0.30	3.73 ± 0.19	1.4
			Demoted from anomaly status				
38	CSS_J123713.5−114008	0.52	EW	RR Lyrae (RRab)	1.56 ± 0.19	1.58 ± 0.17	1.2
178	AQ Ind	2.28	EA	Eclipsing binary (EA)	4.33 ± 0.22	4.34 ± 0.22	0.8
195	UU Oph	4.40	EA/SD	Eclipsing binary (EA)	2.49 ± 1.15	2.59 ± 1.24	0.4

NOTE—Columns as in Table 3. Ranks continue the same ordering, which spans all 276 candidates entering the consensus review.

Multiple inexpensive agents offer a practical purity–cost compromise, but they cannot recover anomalies never proposed for review.

embeddings organized the variable stars in our sample by morphology, with different classes occupying distinct regions (Figures 2 and 3). While fine-tuned visual embeddings have previously been shown to rival time-series representations in variable star classification (D. Moreno-Cartagena et al. 2025), our results demonstrate a successful transfer of pre-trained embeddings in the unsupervised regime. The DINOv2 representation also proved robust to arbitrary phase zero-points and the central preprocessing crop that discards the outermost 6.25% of the image (Appendix C), indicating that the success of the transfer does not hinge on rendering details.

5.2. *LLM Judges*

Of the 43 anomaly labels assigned by the Gemini 3 Flash agents in the main loop and the logistic regression step, the consensus review demoted 23 of them, while elevating 4 potentially interesting objects to anomaly status. We manually inspected all surviving anomalies and overturned sources and found the majority-vote relevance scores to be generally consistent with our own assessments (Section 4.2). Removing the demoted sources therefore increased the purity of the anomaly sample (fraction passing our inspection) by a factor of ∼2. Since the five-agent review targeted only candidates that received $y \geq 1$ in the single-agent stages (5.4% of the labeled set), this increase came at a modest ≈25% additional cost.

Consensus roughly doubled anomaly-sample purity for only about 25% additional cost.

Purity can alternatively be improved by employing a more capable LLM. However, we show it can be considerably more expensive. For example, assuming the same token usage, Gemini 3.1 Pro would increase the labeling cost of the main loop and the logistic regression step by a factor of ∼4 compared to Gemini 3 Flash. Aggregating votes from multiple weaker agents for a small set of flagged sources is therefore more cost-efficient than having all sources evaluated by a single stronger agent. However, stronger agents might still be required when the priority is completeness (recovered fraction of all anomalies in the sample) rather than purity, since the consensus review cannot recover anomalies that were not flagged during the single-agent stages.

5.3. *Agentic Active Learning*

Placing our Gemini 3 Flash agents within an active learning loop greatly reduced the number of sources they needed to review. The agents labeled only ∼1% of the sample but surfaced anomalies across the full range of the initial ranking, with some ranked as low as 3.5×10^5. Reaching these sources under the fixed unsupervised isolation-forest ranking would have required ∼70 times our labeling budget of 5 100 sources. At the same budget, only 30% of our final catalog would have been recovered (Section 4.3), demonstrating the importance of active learning for both extending the reach and increasing the yield of anomaly searches.

5.4. *Scalability*

Together, the active learning loop, logistic regression step, and consensus review finished in roughly 3 hours. The agents labeled 5 100 sources and performed consensus review of 276 anomaly candidates at a total cost of approximately $40 in API calls. The low cost permits scaling to much larger data sets, but active learning rarely requires more than a few thousand labels. For example, V. Etsebeth et al. (2024) found that the anomaly yield diminished rapidly beyond 6 000 labeled samples in their data set of ∼4 million galaxy images. The natural direction for scaling is therefore across multiple data sets rather than within a single large sample. Our pipeline is well aligned with this strategy, as pre-trained visual embeddings and off-the-shelf LLM agents make it readily applicable to other variable-star samples (e.g., X. Chen et al. 2020; A. N. Heinze et al. 2018; I. Soszyński et al. 2016), requiring no fine-tuning or adaptation beyond prompt modification. With a labeling budget similar to ours, the cost of processing each additional data set should stay within a few tens of dollars.

The full agentic workflow took roughly three hours and about $40 in API calls.

More generally, agentic active learning has potential applications in settings that require expert judgment across large samples, such as source classification, artifact identification, and rare-event searches. A predictive model trained on a small agent-annotated subset can extend the labels to the entire data set at a fraction of the cost of exhaustive review. The approach could be especially valuable in applications where expertise is scarce or the task must be repeated regularly. For example, assuming a generous labeling budget of 10^4 sources and per-call API costs comparable to those of our pipeline, an agentic active learning loop applied to the 10^6–10^7 nightly alerts expected from LSST (Ž. Ivezić et al. 2019) could prioritize the most anomalous events for spectroscopic follow-up at $\lesssim$\$100 per night.

5.5. *Limitations*

The most fundamental limitation of our pipeline is representational. Although visual embeddings proved effective at capturing the morphology of phase-folded periodic light curves, this representation does not readily extend to aperiodic sources or transients. One alternative is to embed raw photometry directly using a pre-trained time-series foundation model, but these models typically assume regular sampling, which is rarely the

Figure 11 shows out-of-budget anomalies recovered through neighbor propagation and logistic regression.

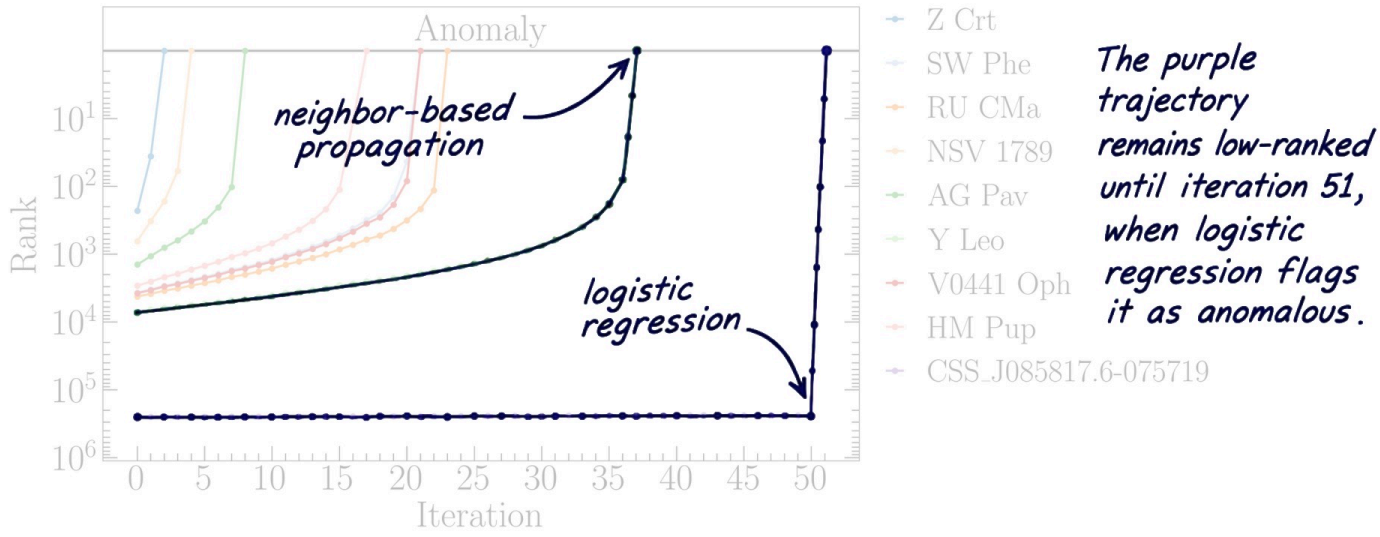


Figure 11. Rank trajectories of the nine unanimously voted anomalies (ranks 1–9 in Table 3) as a function of completed iterations, with the highest-ranked sources at the top. In each iteration, the agents labeled the 100 top-ranked sources from the unlabeled pool. The intersection of each trajectory with the black horizontal line labeled "Anomaly" marks the iteration at which the source was flagged as an anomaly in the initial single-agent stages. Iteration 51 corresponds to the logistic regression step. Two of the nine anomalies have initial ranks (iteration 0) outside our labeling budget of 5 100 sources and were found only through neighbor-based label propagation (Y Leo, rank 6 942) or the logistic regression step (CSS_J085817.6−075719, rank 250 222).

case for light curves. Despite this, W. Li et al. (2025) found that `Chronos-Bolt-tiny`[§], a transformer-based model trained on 100 billion non-astronomical time-series observations, outperformed hand-crafted features in out-of-distribution detection on a sample of 40 000 ZTF variable-star light curves, even without any explicit treatment of the irregular sampling. Time-series foundation models therefore present a promising path for [illegible] streams and near-real-time identification of anomalous events.

Phase-folded images limit the method to periodic behavior; time-series models could extend it to non-periodic sources.

A second major limitation is the lack of external tools available to the agents during evaluation. While we deliberately chose this minimal design to keep our proof-of-concept pipeline simple, equipping the agents with tools for light-curve modeling, outlier detection, or database queries would allow them to gather additional evidence beyond the image and help them make better-informed decisions. Additionally, access to a retrieval-augmented generation (RAG) knowledge base of extended class descriptions, example light curves, and relevant literature [illegible] edge on each class without bloating the prompt. Used selectively when the image alone is inconclusive, these tools could improve the reliability of agent evaluations at modest additional cost.

External tools and retrieval could add evidence when an image is inconclusive. These are proposed extensions.

Several additional design choices also constrain the pipeline. We used isolation forests for the initial ranking, but other methods, such as the local outlier factor (M. M. Breunig et al. 2000) or the sum of the distances to the k nearest neighbors (F. Angiulli & C. Pizzuti 2002), might have produced more informative rankings and increased the anomaly yield. We plotted the V- and g-band light curves in a single image, which biased the estimates of the V-band eclipse depths in EA-type binaries when the light curves overlapped (Section 4.2). Rendering the two bands separately would likely remove this bias. Finally, all evaluations relied on Gemini 3 Flash, a proprietary model that imposes strict API rate limits and ties per-call costs to commercial pricing. Migrating to a locally hosted open-weight multimodal LLM, such as Qwen3-VL (S. Bai et al. 2025) or Gemma 4 (Gemma Team et al. 2026), would remove the API-imposed limits and reduce the cost to that of the compute needed to run the model.

Despite these constraints, the pipeline identified 24 anomalies, including 6 previously studied systems. The agents were not provided with the object names or coordinates and had access to no information beyond what Gemini 3 Flash was trained on, so they flagged these sources based on the light-curve images and metadata alone, making their recovery an independent validation

[§] https://huggingface.co/amazon/chronos-bolt-tiny

Agentic active learning offers a practical route to anomaly detection in large photometric surveys.

of the pipeline. However, this does not let us assess the completeness of our final anomaly sample since we have no record of anomalies that were not recovered by the pipeline.

The most direct next step is to apply the pipeline to variable-star samples from other surveys, such as ZTF (X. Chen et al. 2020), TESS (H. Qiang et al. 2025), and OGLE (I. Soszyński et al. 2016), which would require only rendering their light curves as images. In future work, we plan to address the limitations outlined above and deploy an enhanced version of the pipeline on live alert streams from ZTF and LSST, where it would act as an automated triage layer, surfacing the most anomalous events each night for spectroscopic follow-up.

Planned live ZTF and LSST triage would surface the most anomalous nightly events for spectroscopic follow-up.

6. CONCLUSIONS

In this work, we presented an agentic active learning framework for anomaly detection in photometric samples of periodic variable stars (Figure 1). The pipeline embeds phase-folded light-curve images with the self-supervised DINOv2 vision transformer (Section 3.1), derives a baseline anomaly ranking from class-conditional isolation forests (Section 3.2), refines it through an active learning loop in which Gemini 3 Flash agents label the top-ranked candidates, and propagates the labels to neighboring sources in the embedding space (Section 3.3). A logistic regression step then surfaces anomalies outside these neighborhoods (Section 3.4), and all flagged candidates are re-evaluated by five independent agents in a consensus review (Section 3.5).

Applied to over 370 000 periodic variable stars from ASAS-SN Sky Patrol V2.0, the pipeline identified 24 anomalies and 153 potentially interesting objects among the 5 100 sources labeled by the agents (∼1% of the full sample) across 50 active learning iterations and a single logistic regression step. Our main findings are as follows:

- By our own classification, the anomalies comprise 10 EA-type eclipsing binaries with extremely deep primary eclipses, 7 contact binaries, 3 RRab variables, and 2 Cepheids in the high-amplitude tail of their classes, a deeply eclipsing nova-like system, and an eclipsing symbiotic nova that has been in outburst for over two decades (Section 4.2).
- Six of the anomalies have previously been studied for their unusual properties, while the remaining 18 are new discoveries requiring spectroscopic follow-up to determine their physical nature (Section 4.2.7). Among the latter, 6 were unanimously voted anomalous in the consensus review, making them high-priority targets for follow-up (Section 4.2).

Six anomalies were previously studied; 18 are new discoveries requiring spectroscopic follow-up.

- Without fine-tuning or label supervision, the DINOv2 embeddings organized our sample of variable stars by light-curve morphology, demonstrating successful zero-shot transfer from natural images (Sections 3.1 and 5.1).
- The multi-agent consensus review proved essential for correcting individual agent mistakes, demoting 36% of the positive single-agent labels and roughly doubling the purity of our final anomaly sample (Sections 4.1, 4.2.6, and 5.2).
- The logistic regression step extended the reach of the pipeline beyond neighbor-based propagation, contributing 29% of the anomalies and 19% of the potentially interesting objects in our final catalog (Section 4.1).
- Labeling only ∼1% of the sample, the agents found anomalies initially ranked as low as 3.5×10^5, which would have required ∼70 times our labeling budget to reach them under the fixed unsupervised ranking. At the same budget, only 42% of the anomalies and 28% of the potentially interesting objects from our final catalog would have been recovered (Sections 4.3 and 5.3).
- The agentic stages of the pipeline finished in roughly 3 hours at a total cost of ≈$40 in API calls. The pipeline can be readily applied to other variable-star samples at a comparable cost, requiring no fine-tuning or adaptation beyond prompt modification (Section 5.4).

These results establish our agentic active learning framework as a practical route to anomaly detection in large photometric surveys, although several limitations remain, namely the reliance on phase-folded images, the absence of external tools available to the agents, and the dependence on a proprietary LLM backend imposing strict API rate limits (Section 5.5). In future work, we plan to address these limitations and extend the pipeline to unphased light curves, which will bring aperiodic sources and transients within scope. We also plan to deploy the pipeline on live alert streams from ZTF and LSST.

The planned extension is to unphased light curves, bringing aperiodic sources and transients within scope.

ACKNOWLEDGMENTS

The research of MP was supported by the Czech Science Foundation (GACR) Project No. 25-16846O. YST was supported by NSF Grant AST-2406729 and a Humboldt Research Award from the Alexander von Humboldt Foundation. We thank Chris Kochanek for detailed comments on the manuscript and Camber Inc. for helpful discussions on this project. We also thank

the ASAS-SN team for making their light curves publicly available through Sky Patrol V2.0. This research has made use of the SIMBAD database, CDS, Strasbourg Astronomical Observatory, France (M. Wenger et al. 2000), and of NASA's Astrophysics Data System Bibliographic Services. We acknowledge the use of various versions of GPT (OpenAI), Gemini (Google), and Claude (Anthropic) AI agents for literature review, code development, prompt design, and manuscript preparation. All content was reviewed and verified by the authors, who take full responsibility for the accuracy of this work.

Facility: ASAS-SN

Software: `Matplotlib` (J. D. Hunter 2007), `NumPy` (C. R. Harris et al. 2020), `pandas` (T. pandas development team 2026), `PyTorch` (A. Paszke et al. 2019), `scikit-learn` (F. Pedregosa et al. 2011), `SciPy` (P. Virtanen et al. 2020), `seaborn` (M. L. Waskom 2021), `SkyPatrol` (K. Hart et al. 2023), `Transformers` (T. Wolf et al. 2019), `UMAP` (L. McInnes et al. 2018)

REFERENCES

Angiulli, F., & Pizzuti, C. 2002, in Principles of Data Mining and Knowledge Discovery, ed. T. Elomaa, H. Mannila, & H. Toivonen (Berlin, Heidelberg: Springer Berlin Heidelberg), 15–27

Ashbrook, J. 1950, AJ, 55, 62, doi: 10.1086/106437

Bai, S., Cai, Y., Chen, R., et al. 2025, arXiv e-prints, arXiv:2511.21631, doi: 10.48550/arXiv.2511.21631

Bellm, E. C., Kulkarni, S. R., Graham, M. J., et al. 2019, PASP, 131, 018002, doi: 10.1088/1538-3873/aaecbe

Bird, J. C., Stanek, K. Z., & Prieto, J. L. 2009, ApJ, 695, 874, doi: 10.1088/0004-637X/695/2/874

Boyd, D. 2023, JAAVSO, 51, 74, doi: 10.48550/arXiv.2307.03677

Breunig, M. M., Kriegel, H.-P., Ng, R. T., & Sander, J. 2000, SIGMOD Rec., 29, 93–104, doi: 10.1145/335191.335388

Carson, T. R., & Stothers, R. B. 1984, ApJ, 281, 811, doi: 10.1086/162159

Chen, X., Wang, S., Deng, L., et al. 2020, ApJS, 249, 18, doi: 10.3847/1538-4365/ab9cae

Christy, C. T., Jayasinghe, T., Stanek, K. Z., et al. 2023, MNRAS, 519, 5271, doi: 10.1093/mnras/stac3801

Debosscher, J., Sarro, L. M., Aerts, C., et al. 2007, A&A, 475, 1159, doi: 10.1051/0004-6361:20077638

Etsebeth, V., Lochner, M., Walmsley, M., & Grespan, M. 2024, MNRAS, 529, 732, doi: 10.1093/mnras/stae496

Ferber, D., Wölflein, G., Wiest, I. C., et al. 2024, Nature Communications, 15, 10104, doi: 10.1038/s41467-024-51465-9

Gemma Team, El Abd, S., Aggarwal, V., et al. 2026, arXiv e-prints, arXiv:2607.02770, doi: 10.48550/arXiv.2607.02770

Giuricin, G., Mardirossian, F., & Predolin, F. 1980, Information Bulletin on Variable Stars, 1786, 1

Groenewegen, M. A. T., & Lub, J. 2023, A&A, 676, A136, doi: 10.1051/0004-6361/202346062

Hambsch, F.-J., Hümmerich, S., Bernhard, K., & Otero, S. 2015, JAAVSO, 43, 213, doi: 10.48550/arXiv.1512.01467

Han, X. L., Zhang, L.-Y., Shi, J.-R., et al. 2018, Research in Astronomy and Astrophysics, 18, 068, doi: 10.1088/1674-4527/18/6/68

Harris, C. R., Millman, K. J., van der Walt, S. J., et al. 2020, Nature, 585, 357, doi: 10.1038/s41586-020-2649-2

Hart, K., Shappee, B. J., Hey, D., et al. 2023, arXiv e-prints, arXiv:2304.03791, doi: 10.48550/arXiv.2304.03791

He, K., Chen, X., Xie, S., et al. 2021, arXiv e-prints, arXiv:2111.06377, doi: 10.48550/arXiv.2111.06377

Heinze, A. N., Tonry, J. L., Denneau, L., et al. 2018, AJ, 156, 241, doi: 10.3847/1538-3881/aae47f

Hewish, A., Bell, S. J., Pilkington, J. D. H., Scott, P. F., & Collins, R. A. 1968, Nature, 217, 709, doi: 10.1038/217709a0

Hinton, G. E., & Salakhutdinov, R. R. 2006, Science, 313, 504, doi: 10.1126/science.1127647

Hümmerich, S., Otero, S., Tisserand, P., & Bernhard, K. 2015, JAAVSO, 43, 14, doi: 10.48550/arXiv.1501.05154

Hunter, J. D. 2007, Computing in Science and Engineering, 9, 90, doi: 10.1109/MCSE.2007.55

Ishida, E. E. O., Beck, R., González-Gaitán, S., et al. 2019, MNRAS, 483, 2, doi: 10.1093/mnras/sty3015

Ishida, E. E. O., Kornilov, M. V., Malanchev, K. L., et al. 2021, A&A, 650, A195, doi: 10.1051/0004-6361/202037709

Ivezić, Ž., Kahn, S. M., Tyson, J. A., et al. 2019, ApJ, 873, 111, doi: 10.3847/1538-4357/ab042c

Jayasinghe, T., Kochanek, C. S., Stanek, K. Z., et al. 2021, MNRAS, 503, 200, doi: 10.1093/mnras/stab114

Jia, M., Zhang, Q., Luo, A., et al. 2026, arXiv e-prints, arXiv:2601.06498, doi: 10.48550/arXiv.2601.06498

Jimenez Rezende, D., & Mohamed, S. 2015, arXiv e-prints, arXiv:1505.05770, doi: 10.48550/arXiv.1505.05770

Kim, D.-W., & Bailer-Jones, C. A. L. 2016, A&A, 587, A18, doi: 10.1051/0004-6361/201527188
Kjurkchieva, D., Khruzina, T., Dimitrov, D., et al. 2015, A&A, 584, A40, doi: 10.1051/0004-6361/201526102
Kochanek, C. S., Shappee, B. J., Stanek, K. Z., et al. 2017, PASP, 129, 104502, doi: 10.1088/1538-3873/aa80d9
Leavitt, H. S., & Pickering, E. C. 1912, Harvard College Observatory Circular, 173, 1
Leoni, M., Ishida, E. E. O., Peloton, J., & Möller, A. 2022, A&A, 663, A13, doi: 10.1051/0004-6361/202142715
Li, W., Chen, H.-Y., Rehemtulla, N., et al. 2025, arXiv e-prints, arXiv:2510.06200, doi: 10.48550/arXiv.2510.06200
Liakos, A., Moriarty, D. J. W., Blackford, M. G., et al. 2022, A&A, 663, A137, doi: 10.1051/0004-6361/202243313
Liang, Y., Melchior, P., Lu, S., Goulding, A., & Ward, C. 2023, AJ, 166, 75, doi: 10.3847/1538-3881/ace100
Liu, F. T., Ting, K. M., & Zhou, Z.-H. 2008, in 2008 Eighth IEEE International Conference on Data Mining (IEEE), 58, doi: 10.1109/ICDM.2008.17
Lochner, M., & Bassett, B. A. 2021, Astronomy and Computing, 36, 100481, doi: 10.1016/j.ascom.2021.100481
Lochner, M., & Rudnick, L. 2025, AJ, 169, 121, doi: 10.3847/1538-3881/ada14c
McInnes, L., Healy, J., & Melville, J. 2018, arXiv e-prints, arXiv:1802.03426, doi: 10.48550/arXiv.1802.03426
Moreno-Cartagena, D., Protopapas, P., Cabrera-Vives, G., et al. 2025, A&A, 703, A41, doi: 10.1051/0004-6361/202554289
Moriarty, D. J. W., Bohlsen, T., Heathcote, B., Richards, T., & Streamer, M. 2013, JAAVSO, 41, 182
Nicolaou, C., Nathan, R. P., Lahav, O., et al. 2026, MNRAS, 547, stag010, doi: 10.1093/mnras/stag010
Oquab, M., Darcet, T., Moutakanni, T., et al. 2023, arXiv e-prints, arXiv:2304.07193, doi: 10.48550/arXiv.2304.07193
pandas development team, T. 2026, pandas-dev/pandas: Pandas, v3.0.5 Zenodo, doi: 10.5281/zenodo.21500199
Paszke, A., Gross, S., Massa, F., et al. 2019, arXiv e-prints, arXiv:1912.01703, doi: 10.48550/arXiv.1912.01703
Pedregosa, F., Varoquaux, G., Gramfort, A., et al. 2011, Journal of Machine Learning Research, 12, 2825, doi: 10.48550/arXiv.1201.0490
Pešta, M., & Pejcha, O. 2023, A&A, 672, A176, doi: 10.1051/0004-6361/202245613
Pop, A., Turcu, V., & Marcu, A. 2011, Ap&SS, 333, 17, doi: 10.1007/s10509-011-0627-8
Pruzhinskaya, M. V., Ishida, E. E. O., Novinskaya, A. K., et al. 2023, A&A, 672, A111, doi: 10.1051/0004-6361/202245172
Qiang, H., Kounkel, M., Bass, S., et al. 2025, ApJ, 984, 49, doi: 10.3847/1538-4357/adc2fc
Radford, A., Kim, J. W., Hallacy, C., et al. 2021, arXiv e-prints, arXiv:2103.00020, doi: 10.48550/arXiv.2103.00020
Richards, J. W., Starr, D. L., Brink, H., et al. 2012, ApJ, 744, 192, doi: 10.1088/0004-637X/744/2/192
Schmidt, E. G., Lee, K. M., Johnston, D., Newman, P. R., & Snedden, S. A. 2003, AJ, 126, 906, doi: 10.1086/376845
Schmidt, M. 1963, Nature, 197, 1040, doi: 10.1038/1971040a0
Shappee, B. J., Prieto, J. L., Grupe, D., et al. 2014, ApJ, 788, 48, doi: 10.1088/0004-637X/788/1/48
Simon, N. R., & Lee, A. S. 1981, ApJ, 248, 291, doi: 10.1086/159153
Smak, J. 2019, AcA, 69, 79, doi: 10.32023/0001-5237/69.1.6
Soszyński, I., Pawlak, M., Pietrukowicz, P., et al. 2016, AcA, 66, 405, doi: 10.48550/arXiv.1701.03105
Stoppa, F., Bulmus, T., Bloemen, S., et al. 2025, Nature Astronomy, 9, 1869, doi: 10.1038/s41550-025-02670-z
Subebekova, G., Zharikov, S., Tovmassian, G., et al. 2020, MNRAS, 497, 1475, doi: 10.1093/mnras/staa2091
Tonry, J. L., Denneau, L., Flewelling, H., et al. 2018, ApJ, 867, 105, doi: 10.3847/1538-4357/aae386
Turcu, V., Pop, A., Marcu, A., & Moldovan, D. 2011, Ap&SS, 331, 105, doi: 10.1007/s10509-010-0432-9
Villar, V. A., Cranmer, M., Berger, E., et al. 2021, ApJS, 255, 24, doi: 10.3847/1538-4365/ac0893
Virtanen, P., Gommers, R., Oliphant, T. E., et al. 2020, Nature Methods, 17, 261, doi: 10.1038/s41592-019-0686-2
Vojkhanskaya, N. F. 1984, AZh, 61, 1137
Waskom, M. L. 2021, Journal of Open Source Software, 6, 3021, doi: 10.21105/joss.03021
Wenger, M., Ochsenbein, F., Egret, D., et al. 2000, A&AS, 143, 9, doi: 10.1051/aas:2000332
Wolf, T., Debut, L., Sanh, V., et al. 2019, arXiv e-prints, arXiv:1910.03771, doi: 10.48550/arXiv.1910.03771
Xu, X., Wang, H., Liang, Y., et al. 2025, arXiv e-prints, arXiv:2502.17812, doi: 10.48550/arXiv.2502.17812
Yacob, A. M., Berdnikov, L. N., Pastukhova, E. N., Kniazev, A. Y., & Whitelock, P. A. 2022, MNRAS, 516, 2095, doi: 10.1093/mnras/stac2167

The appendix documents the agent prompt and finds consistent reasoning and robust embeddings.

APPENDIX

A. PROMPT

All agent evaluations in the active learning loop (Section 3.3), logistic regression step (Section 3.4), and consensus review (Section 3.5) relied on a single prompt implementing eight sequential steps: visual inspection, data quality checks, amplitude estimation, classification, extreme-parameter flagging, scoring, self-audit, and structured JSON response. Figure 12 presents a condensed version of the full 1 460-word prompt, which is available in our GitHub repository (https://github.com/milanpesta/aal_anomalies_asassn).

B. AGENT REASONING CONSISTENCY

To verify that the reasoning of the agents was consistent with the assigned relevance scores, we performed an n-gram frequency analysis of the rationales from the consensus review. For each source, we collected the rationales of the agents whose individual scores matched the majority relevance label. We converted all text to lowercase, removed non-alphabetic characters and stop words (e.g., "the", "and", "with"), discarded words shorter than three characters, and compiled the set of unique n-grams for each source so that a term repeated across rationales counted only once. We also recorded the unique diagnostic flags that the agents raised during their analysis of each source, providing an independent reference against which to compare the vocabulary of the rationales. Table 5 reports the five most frequent unigrams, bigrams, and trigrams along with the triggering rates of selected diagnostic flags for each of the three relevance scores.

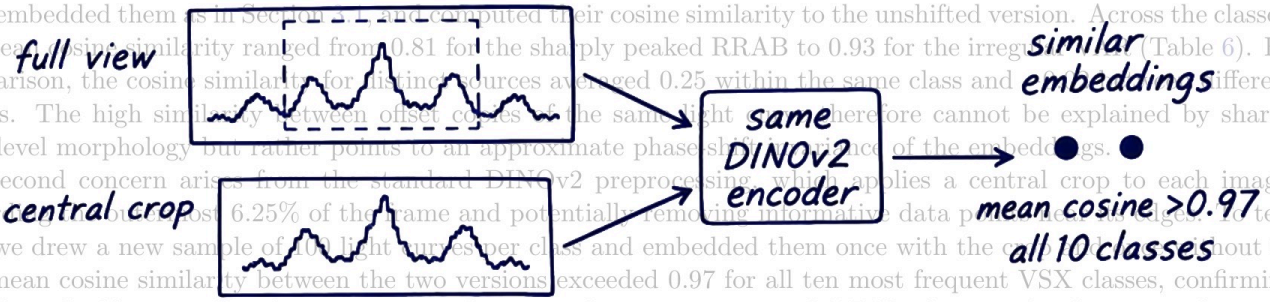
Rationale words agree with diagnostic flags: evidence of internal consistency, not an independent accuracy test.

The [illegible] the agents' rationales and the [illegible] the flags. For the most relevant sources, the most frequent words are "exceeding" (91.7%) and "extreme" (83.3%), which is consistent with the flag analysis, where all anomalies triggered `extreme_amplitude` and no data quality flags were raised. For the 153 potentially interesting objects, the vocabulary shifts to "boundary" (81.0%) and "near" (79.1%), in line with `amplitude_near_boundary` being raised for 89.5% of them, while `extreme_amplitude` was triggered for only 1.3%. The rationales for the 99 demoted sources split between overlooked data quality issues and incorrectly flagged sources that are standard for their class, with "quality" appearing for 78.8% of the demoted sources and "standard" for 72.7%. The flag analysis shows the same split, with 56.6% of the sources triggering `data_quality_issues`. Overall, each relevance label carries a distinct vocabulary that aligns well with its flag signature, confirming that the agents were internally consistent in their decision process.

C. EMBEDDING ROBUSTNESS

The phase of each light curve is measured from an arbitrary initial epoch, which introduces a relative phase offset between light curves of the same class. To quantify how [illegible] the DINOv2 embeddings, we selected 100 randomly selected light curves from each of the ten most common VSX classes at phase offsets spanning the full cycle in steps of 0.05, embedded them as in Section 3.2, and computed their cosine similarity to the unshifted version. Across the classes, the mean cosine similarity ranged from 0.81 for the sharply peaked RRAB to 0.93 for the irregular L (Table 6). By comparison, the cosine similarity for distinct sources averaged 0.25 within the same class and [illegible] between different classes. The high similarity between offset copies of the same light curve therefore cannot be explained by shared class-level morphology but rather points to an approximate phase shift [illegible] of the embeddings.

Different views, nearly the same representation.



A second concern arises from the standard DINOv2 preprocessing, which applies a central crop to each image, discarding the outer [illegible] most 6.25% of the frame and potentially removing informative data present in wide-field images. To test this, we drew a new sample of 100 light curves per class and embedded them once with the crop and once without it. The mean cosine similarity between the two versions exceeded 0.97 for all ten most frequent VSX classes, confirming that the embeddings are largely insensitive to the crop. This is consistent with DINOv2's image-level training objective, which aligns the `[CLS]` token across global and local views and encourages approximate invariance to cropping (M. Oquab et al. 2023).

Phase-shifted copies are much more similar than distinct stars from the same class.

Figure 12 condenses the ordered agent prompt for evaluating anomaly candidates.


```
You are an astrophysical time-series and variable star expert. Analyze a single phased light curve, assign discrete
relevance score 0, 1, or 2 based on how anomalous AND astrophysically relevant the light curve appears. Return ONE JSON
ONLY—no prose/markdown/fences.

INPUTS:id(str),period_days(days),y_scale_mag(mag),catalog_label(str),image(518×518px;filters:V=blue,g=green;gridlines=gray)
IMAGE GUIDANCE
axes:X=phase[−0.5,+0.5],Y=inverted mag(bright=TOP,faint=BOTTOM,span=y_scale_mag);blue may hide behind green
grid:20x20;1 col=0.05 phase,1 row=y_scale_mag/20

STEPS:0)Visual inspection 1)Data+folding+morphology checks 2)Amplitude 3)Class 4)Extreme flags 5)Score 6)Audit 7)JSON
PRIORITIES:Detect quality/systematic issues;keep scores conservative when quality concerns exist

STEP 0:VISUAL INSPECTION(≤200w,skeptically describe what you see)
1.Global:dense/sparse,clean/noisy,filters(V&g),outliers,repeating shapes
[...5 further inspection items and guidelines...]
Output JSON fields:raw_visual_description

STEP 1:CHECKS
SKEPTICAL DEFAULTS:Issues=True,Positive attributes=False;overturn only with clear visual evidence
AGGREGATION:"V OR g"(evaluate per filter,True if either);"MAX"(evaluate per filter,report highest);[...]

|Check|Type|Agg|Rule|
|has_V_filter|bool|—|≥1 data point in V|
[...21 further checks...]
Output JSON fields:all filters+data_quality+folding+morphology checks

STEP 2:AMPLITUDE(Vertical extent of V&g backbones;NOT absolute position)
Per filter:
1)ID backbone:find coherent phase-correlated structure;exclude vertically spread phase-independent scatter[...]
[...3 further amplitude steps and guidelines...]
Output JSON fields:inferred_V_amplitude_mag,inferred_g_amplitude_mag

STEP 3:CLASSIFICATION
Allowed:RR_Lyrae_ab|RR_Lyrae_c|[...24 further classes...]|unknown

CLASS TABLE(P=period days,A=amplitude mag):
|Class|P|A|Neg(exclude)|Pos(support)|
|RR_Lyrae_ab|0.3-1.2|0.5-1.3|2 max+2 min;flat top;double-wave;LPV-broad min|Sharp sawtooth;1 max+1
min;fast↑slow↓;asym~0.5-0.9;mod~0-0.5|
[...26 further classes...]

Critical rules:>2 min→LPV/irregular NOT eclipsing;[...]

Synonyms(non-exhaustive,case-insensitive):
E,E/RS→eclipsing_binary_EA,eclipsing_binary_EB,contact_binary
[...28 further synonym rows and label-interpretation notes...]

CATALOG_LABEL SYMBOL CONVENTIONS:
|(pipe)=logical OR;uncertain classification,all possible types indicated(e.g.,ELL|DSCT=ellipsoidal OR delta_Scuti)
[...4 further symbols and parsing rule...]

Process:
1)catalog_label_interpreted:parse symbols(|,+,/,!);map each component via synonyms(sep with commas);[...]
[...5 further process steps...]
Output JSON fields:catalog_label_interpreted,possible_classes,inferred_variability_type,type_match

STEP 4:EXTREME FLAGS
|Flag|Rule|
|extreme_amplitude|A>1.1×upper for class AND data_quality_issues=False;compare both V&g vs class A-range;[...]|
[...7 further flags...]

Process:
1)Get P&A ranges for inferred_variability_type from Step 3 CLASS TABLE
[...2 further process steps...]
Output JSON fields:calculations(document all arithmetic),all extreme+boundary+mixed flags

STEP 5:SCORING(Evaluate anchors in order;STOP at first match)
BINS:0=not_interesting,1=potentially_interesting,2=anomaly
[...2 definitions...]

|Priority|Condition|Score|
|1|folded_correctly=False|0|
[...7 further anchors...]

SCORING LOGIC:
Priority 1-2:Folding/quality issues→0
[...6 further anchor descriptions and 2 scoring notes...]
Output JSON fields:relevance_score,label,confidence,rationale

STEP 6:AUDIT(verify STEPS 0-5 again before generating JSON,check for mistakes)
0.Visual inspection:raw_visual_description complete? [...]
[...5 further audit items...]

STEP 7:JSON SCHEMA(output raw JSON only)
{
  "meta":{[...4 metadata fields...]},
  "analysis":{[...8 analysis field groups...]},
  "results":{
    "relevance_score":"<0|1|2>",
    "label":"<not_interesting|potentially_interesting|anomaly>",
    [...2 further fields...]
  }
}

VALIDATION:Numeric in range;relevance_score must be 0,1,or 2(int);strings match allowed;[...]
```

The output is raw JSON, with checked numeric ranges and allowed labels.

Figure 12. Condensed version of the prompt used by the agents when evaluating anomaly candidates. Bracketed ellipses mark omissions. Retained text is verbatim.

Failed folding gets score 0; folding and quality checks take priority over anomaly scoring.

The words agents used match the intended three-way distinction: extreme, near-boundary, or often compromised by quality.

Only outputs from agents whose individual scores matched the consensus label are included.

Table 5. Top five unigrams, bigrams, and trigrams in the agent rationales and triggering rates of selected diagnostic flags for each consensus relevance label.

	Anomaly	Potentially interesting	Not interesting
Unigrams	amplitude (100%) mag (95.8%) exceeding (91.7%) extreme (83.3%) high (83.3%)	class (92.8%) amplitude (92.2%) boundary (81.0%) near (79.1%) morphology (74.5%)	quality (78.8%) extreme (72.7%) standard (72.7%) binary (68.7%) features (67.7%)
Bigrams	exceeding standard (70.8%) exceeding typical (66.7%) high amplitude (62.5%) mag significantly (62.5%) extreme amplitude (58.3%)	amplitude near (71.9%) near upper (52.3%) boundary class (51.0%) morphology amplitude (45.1%) high amplitude (43.8%)	quality issues (62.6%) data quality (61.6%) anomalous features (49.5%) period amplitude (49.5%) eclipsing binary (36.4%)
Trigrams	mag exceeding standard (41.7%) mag significantly exceeding (33.3%) mag significantly exceeds (33.3%) significantly exceeding typical (33.3%) significantly exceeding standard (29.2%)	amplitude near upper (46.4%) physical limit class (28.8%) classic contact binary (26.1%) near upper physical (25.5%) upper physical limit (24.8%)	data quality issues (49.5%) typical period amplitude (30.3%) binary typical period (22.2%) parameters well within (20.2%) standard contact binary (19.2%)
Flags	`extreme_amplitude` (100%) `extreme_period` (4.2%) `amplitude_near_boundary` (4.2%) `period_near_boundary` (4.2%) `outlier_dominated` (0.0%) `data_quality_issues` (0.0%)	`extreme_amplitude` (1.3%) `extreme_period` (0.0%) `amplitude_near_boundary` (89.5%) `period_near_boundary` (6.5%) `outlier_dominated` (0.0%) `data_quality_issues` (0.0%)	`extreme_amplitude` (1.0%) `extreme_period` (0.0%) `amplitude_near_boundary` (2.0%) `period_near_boundary` (1.0%) `outlier_dominated` (51.5%) `data_quality_issues` (56.6%)

Note—The n-grams are ranked by the fraction of objects for which at least one rationale contained them, given in parentheses. Flag percentages give the fraction of objects for which at least one agent raised the flag. Only outputs of agents whose individual scores matched the consensus label are included.

Each phrase counts at most once per object, so repeated uses do not inflate its frequency.

Internal consistency is reassuring, though it is not the same as astrophysical correctness.

DINOv2 embeddings are approximately phase-shift invariant, even for sharply structured periodic light curves.

Table 6. Mean cosine similarity between the DINOv2 embeddings of shifted and unshifted versions of the same light curve, listed by phase offset for the ten most frequent VSX classes.

Phase offset	SR	EW	ROT	EA	RRAB	SRS	MISC	VAR	RRC	EB
0.05	0.923	0.939	0.915	0.909	0.932	0.918	0.947	0.948	0.918	0.926
0.10	0.887	0.923	0.900	0.865	0.886	0.894	0.925	0.933	0.889	0.875
0.15	0.875	0.925	0.879	0.843	0.848	0.875	0.901	0.930	0.862	0.855
0.20	0.856	0.906	0.864	0.814	0.795	0.848	0.909	0.923	0.833	0.829
0.25	0.856	0.898	0.864	0.793	0.764	0.841	0.906	0.918	0.837	0.825
0.30	0.843	0.899	0.847	0.784	0.746	0.849	0.903	0.918	0.826	0.824
0.35	0.836	0.901	0.855	0.791	0.751	0.851	0.905	0.923	0.835	0.830
0.40	0.848	0.912	0.860	0.795	0.756	0.871	0.907	0.929	0.842	0.832
0.45	0.860	0.918	0.856	0.792	0.757	0.862	0.900	0.926	0.849	0.836
0.50	0.849	0.921	0.867	0.828	0.766	0.865	0.902	0.931	0.856	0.838
0.55	0.835	0.922	0.858	0.831	0.782	0.864	0.906	0.928	0.844	0.835
0.60	0.833	0.911	0.863	0.822	0.781	0.857	0.901	0.931	0.837	0.828
0.65	0.817	0.907	0.852	0.809	0.789	0.848	0.894	0.924	0.831	0.813
0.70	0.828	0.893	0.853	0.800	0.794	0.846	0.895	0.910	0.833	0.813
0.75	0.828	0.908	0.854	0.786	0.805	0.849	0.899	0.913	0.843	0.833
0.80	0.842	0.906	0.852	0.792	0.828	0.863	0.907	0.909	0.849	0.830
0.85	0.855	0.913	0.870	0.825	0.851	0.884	0.908	0.921	0.862	0.867
0.90	0.883	0.923	0.884	0.853	0.875	0.897	0.925	0.925	0.884	0.886
0.95	0.922	0.945	0.921	0.918	0.927	0.927	0.942	0.946	0.922	0.919
Mean	0.857	0.914	0.869	0.824	0.812	0.869	0.910	0.926	0.855	0.847

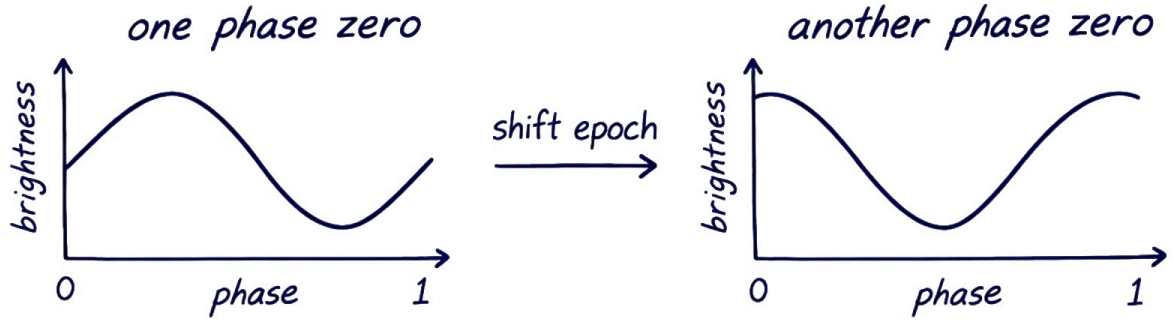
NOTE—Classes are ordered from left to right by decreasing frequency in our sample. Each value is the mean over 100 randomly selected light curves of the corresponding class. All embeddings were centered as in Section 3.1 before computing the cosine similarity. The bottom row gives the mean over all offsets.

average across all phase offsets

lowest

highest

The phase zero-point is arbitrary; changing it should move the curve, not change the star.



similar embeddings, not identical